Modelling and analysis on high sediment concentration layer of fine sediments under wave-dominated conditions

Zuo, Liqin; Roelvink, Dano; Lu, Yongjun; Wang, Hao

Important note
To cite this publication, please use the final published version (if applicable).
Please check the document version above.

Modelling and analysis on high sediment concentration layer of fine sediments under wave-dominated conditions

Liqin Zuo[a,b,d], Dano Roelvink[b,c,d,*], Yongjun Lu[a,**], Hao Wang[b]

[a] State Key Laboratory of Hydrology-Water Resources and Hydraulic Engineering, Nanjing Hydraulic Research Institute, 34 Hujuguan Road, Nanjing, 210024, China
[b] IHE Delft Institute for Water Education, PO Box 3015, 2601, DA, Delft, the Netherlands
[c] Deltares, PO Box 177, 2600, MH, Delft, the Netherlands
[d] Civil Engineering and Geosciences Faculty, Delft University of Technology, PO Box 5048, 2600, GA, Delft, the Netherlands

ABSTRACT

Experiments and field observations have revealed that when silt and very fine sand are subject to oscillatory wave motion, a high shear flow layer and a high concentration layer (HCL) exist near the bottom. The behavior of the HCL is still under researched. Firstly, an intra-wave process based 1DV model was established for fine sediment transport under the combined action of waves and currents. Some key processes that were included in the model are represented through approaches for different bed forms (rippled bed and 'flat bed'), hindered settling, stratification, reference concentration and critical shear stress. A number of experimental datasets were collected to verify the model, which shows that the model is able to properly simulate the flow and sediment dynamics. Secondly, sensitivity analyses were carried out on some factors which would impact the suspended sediment concentration (SSC) profile of the HCL by the 1DV model, such as bed forms, flow dynamics, stratification effects, mobile bed effects and hindered settling. Results show that bed forms play a significant role in the HCL and determination of the shape of the concentration profile. When a current is imposed, the SSC profiles become smoother; however, sediment concentration in the lower HCL is still dominated by the wave motions. For finer sediment, the stratification effects and the mobile bed effects strongly impact the HCL. In conclusion, this paper provides a tool for the study of the HCL and an evaluation of several impact factors on the HCL.

1. Introduction

On the basis of grain size, sediments can be simply classified as gravel ($d > 2\,mm$), sand ($d = 63\,\mu m$–$2\,mm$), silt ($d = 4$–$63\,\mu m$), and clay ($d < 4\,\mu m$). Non-cohesive sand, cohesive mud sediments and even sand-mud mixtures have been studied extensively (e.g., van Rijn, 1993; Ribberink and Al-Salem, 1995; Winterwerp, 2002; Sanford, 2008; Kranenburg et al., 2013; Groenenboom, 2015). However, the behavior of silt-dominated sediments is relatively poorly understood (van Maren et al., 2009). Silt-dominated coastal areas are widely found in the east Bohai Bay and the Jiangsu coast in China. Recent field observations and flume experiments have shown that silt-dominated sediment has special characteristics, neither typical for non-cohesive sand nor for cohesive mud. Silty sediment is easily re-suspended and forms high concentrations near the bottom. Under strong wave conditions it can be stirred up in large volumes, moved by currents and deposited near infrastructure like harbors, waterways, and intakes. Due to its special behavior, this

kind of sediment has drawn much attention from researchers in recent years, such as studies on the hindered settling (Te Slaa et al., 2015), sediment movement (Cao et al., 2009) and reference concentration (Yao et al., 2015).

Silt and very fine sand can be referred to as pseudo-cohesive or semi-cohesive sediment in order to be differentiated from non-cohesive and cohesive materials (Yao et al., 2015). Silt may hold features of both non-cohesive and cohesive sediments, i.e., it is a transitional material from non-cohesive to cohesive sediment. It is natural that there is no clear separation of cohesive and non-cohesive sediments and it is reasonable to have a transition zone between them from a sense of continuity. Silt-enriched mixtures show cohesive-like behavior during erosion tests (Roberts et al., 1998). However, flocculation and consolidation have not been observed in settling experiments (Te Slaa et al., 2013, 2015; Yao et al., 2015). According to laboratory experiments in combination with field work in silt-rich environments (Te Slaa et al., 2013), the transitional behavior in silt-rich sediment occurs at a

threshold when the clay content is about 10%. Mehta and Lee (1994) suggested that the 10–20 μm size may be considered practically to be the dividing size that differentiates cohesive and cohesionless sediment behavior. Tevens (1991) proposed 16 μm to be the division between sediments that flocculate significantly. Some experiments (e.g., Zhou and Ju, 2007; Li, 2014; Yao et al., 2015) showed that the grain size of 45 μm–110 μm shared similar suspension behavior under wave-current conditions. Thus, this study focuses on coarse silt and very fine sand, which is considered to be the transition zone of non-cohesive and cohesive sediments.

One of the most important characteristics of silt and fine sand is a high sediment concentration layer (HCL) that exists near the bed bottom under wave-dominated conditions. The HCL is neither like the fluid mud layer of clay with flocculation and consolidation process nor similar to the intensive bed load transport layer of coarse sand. Sediment suspension is limited by the high oscillatory motion, and the sediment concentration near the bottom is much higher than that in the upper part. The HCL has been found in laboratory experiments (Dohmen Janssen et al., 2001; Yao et al., 2015) and field observations (Te Slaa et al., 2013). Some literature (Trowbridge and Kineke, 1994; Kineke et al., 1996) defines high concentration at the elevation where the concentration $c = 10\,kg/m^3$, or $c = 21\,kg/m^3$ by Winterwerp (1999). Lamb and Parsons (2005) defined the thickness of the high concentrated mud layer as the elevation where the concentration $c = 0.1\,c_{bed}$ (where c_{bed} is arbitrarily set at 1400 g/L). Experiments have shown (Zhou and Ju, 2007; Li, 2014; Yao et al., 2015) that there is a distinct interface between the HCL near the bottom and the clear water in the upper part under wave conditions, as shown in Fig. 1. In this study we define the HCL as the higher concentration layer below where the gradient of sediment concentration changes abruptly in the upper part.

The presence of bed forms, i.e., rippled bed or 'flat bed' (sheet flow), has a large influence on sediment transport (Ribberink and Al Salem, 1994). The eddy viscosity and sediment transport mechanisms are different under different bed forms. For silt and very fine sand, since the bed forms transform easily, the effects of bed forms are more important. Some laboratory experiments have shown that, under gentle conditions, normally $h = 0.3$–0.5 m, $H = 0.1$–0.2 m, the bed forms of silt and very fine sand are rippled beds (Zhou and Ju, 2007; Li, 2014; Yao et al., 2015). Sheet flow is usually present under stronger dynamics. Normally, the criterion of bed forms can be represented by the Shields number or mobility number (Dingler and Inman, 1976; Nielsen, 1992),

$$\psi = \frac{u_{wc}^2}{(s-1)gd_{50}}$$
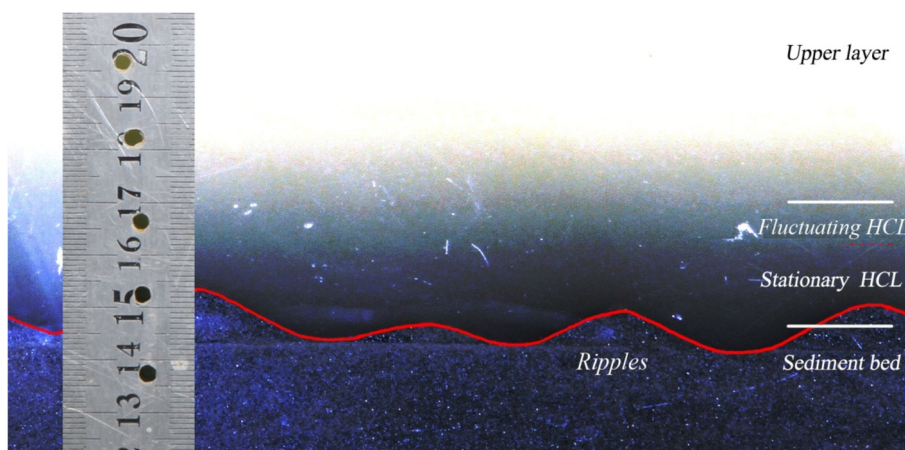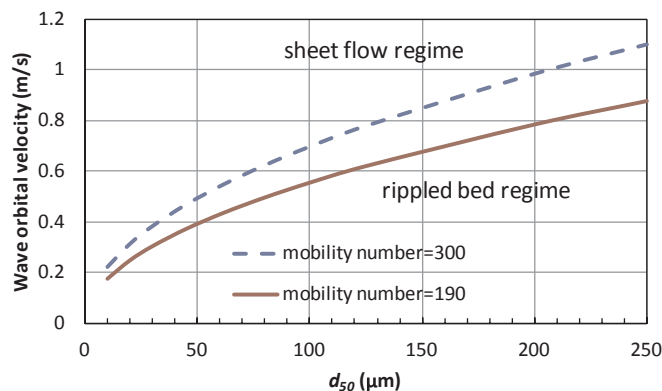
Fig. 2. The criterion conditions of bed forms according to O'Donoghue et al. (2006).

where u_{wc} = the velocity of combined wave-current, $s = 2.65$ = relative density, g = gravity acceleration, and d_{50} = median diameter of sediment grain size. According to O'Donoghue et al. (2006), flat bed (sheet-flow) regime prevails when $\psi > 300$, the ripple regime happens when $\psi < 190$ and a transition regime prevails when $190 < \psi < 300$. Fig. 2 shows the criterion conditions of bed forms according to sediment grain size and wave orbital velocity u_w. It can be seen that, sheet flow only exists in strong dynamics condition for sand (when $u_w > 1.0$ m/s for $d_{50} = 200\,\mu m$), but silt may experience both rippled bed and sheet flow under common conditions (bed type may change when $u_w = 0.30$–0.38 m/s for $d_{50} = 30\,\mu m$). Silt that with smaller grain size than sand is easier to transform from rippled bed to sheet flow. Therefore, the bed form regime is one of the important factors for silt transport. Although some scholars (e.g., Ribberink and Al Salem, 1994; Ribberink et al., 2007) have analyzed the bed forms' influence on sediment transport qualitatively, more studies are needed on the quantitative modeling of turbulence, flow dynamics and sediment dynamics.

In addition to experiments, bottom boundary layer models (normally 1DV) are powerful tools for studying sediment transport mechanisms. A number of numerical models for sediment transport have been developed over the years. Sediment transport modelling was started in the last century with the development of 1DV models (Smith and McLean, 1977; Grant and Madsen, 1979; Grant et al., 1984; Stive and De Vriend, 1994). Because of their simplicity and precision, these models are valuable for some special issues, such as the intra-wave vertical distribution of velocity, shear stress and concentration. Different models have been developed to predict sediment transport under waves or wave-current conditions. These models can be divided into

Fig. 1. High concentration layer (HCL) measured in flume experiment with median sediment grain size of 88 μm (Yao et al., 2015) (The darker color represents higher sediment concentration).

three different classes (Hassan and Ribberink, 2010; Zhang et al., 2011a): empirical quasi-steady transport models, intermediate transport models, and fully unsteady sediment transport models (process based). Fully unsteady sediment transport models are based on a time-dependent simulation of both velocities and concentrations during the wave cycle at different elevations above the bed, such as (Fredsøe, 1984; Ribberink and Al-Salem, 1995; Uittenbogaard et al., 2001; Guizien et al., 2003; Holmedal and Myrhaug, 2006, 2009; Ruessink et al., 2009; Hassan and Ribberink, 2010; Kranenburg et al., 2013). The process-based unsteady models are based on more advanced approaches, and this study focuses on this kind of model. Up until now, there are many models focusing on sand (e.g., Uittenbogaard et al., 2000; Dong et al., 2013; Kranenburg et al., 2013) and fluid mud (e.g., Winterwerp and Uittenbogaard, 1997; Hsu et al., 2009), but few models on silty sediments.

Above all, there is still a lack of thorough modelling and parameterization of the sediment concentration distribution in the HCL of silt and very fine sand. A 1DV model was established which focuses on silt movement and is also applicable to sand. Process descriptions for silt and sand are given in the model, e.g., different bed forms (rippled bed and 'flat bed'), hindered settling, stratification effects, reference concentration and critical shear stress. A number of experimental datasets were collected to validate the model. Sensitivity calculations were carried out with the model to analyze several factors that would impact the sediment concentration profile near the bed bottom. This paper is organized as follows: Section 1 is the introduction; Section 2 provides a description of the 1DV model; Section 3 shows the model verification with experimental data on flow dynamics and sediment concentrations related to sheet flow and rippled beds; Section 4 presents sensitivity calculations and discussions; and Section 5 contains the summary and concluding remarks.

2. 1DV model for flow-sediment movement in wave-current bottom boundary layer

A 1DV model was established for flow dynamics and sediment transport in wave-current bottom boundary layer. The highlights of this model are that special approaches of silty sediment were introduced, and the effects of bed forms are considered in one procedure.

2.1. Governing equations

To simulate the intra-wave process of wave-current and sediment concentration, Reynold equations were employed. Following the Reynold's decomposition method, the Reynolds equations for the wave-current boundary layer can be derived from the N-S equations in x-z coordinates. From the derivation process, it is helpful to understand the wave-current interaction terms. Appendix A provides details. The equations read:

Continuity equation

$$\frac{\partial u}{\partial x} + \frac{\partial w}{\partial z} = 0 \tag{1}$$

Momentum equation

$$\frac{\partial u}{\partial t} + u\frac{\partial u}{\partial x} + w\frac{\partial u}{\partial z} = -\frac{1}{\rho}\frac{\partial p}{\partial x} + \frac{\partial}{\partial z}\left[(\upsilon + \upsilon_t)\frac{\partial u}{\partial z}\right] \tag{2}$$

The equation for sediment concentration c

$$\frac{\partial c}{\partial t} + u\frac{\partial c}{\partial x} + (w - w_s)\frac{\partial c}{\partial z} = \frac{\partial}{\partial z}\left(\varepsilon_s\frac{\partial c}{\partial z}\right) \tag{3}$$

Here u and w are velocities on x and z coordinates, respectively, p is the water pressure, υ is the kinematic viscosity coefficient, υ_t is the eddy viscosity, c is the sediment concentration, ε_s is the sediment diffusivity, and w_s is the settling velocity.

Table 1
Coefficients in the standard $k - \varepsilon$ and NTM turbulence model.

	c_μ	f_μ	$c_{1\varepsilon}$	$c_{2\varepsilon}$	σ_k	σ_ε	f_1	f_2
Standard	0.09	1.0	1.44	1.92	1.0	1.3	1.0	1.0
NTM	0.09	$f_{\mu N}$	1.45	1.90	1.4	1.3	1.0	f_{2N}

Note:
$f_{\mu N} = (1 + 4.1/R_t^{0.75})(1 - \exp(-z^*/15.75))^2$, $f_{2N} = (1 - 0.3\exp(-(R_t/6.5)^2))$.

$\times (1 - \exp(-z^*/3.64))^2$, $R_t = k^2/(\varepsilon\upsilon)$, $z^* = (\upsilon\varepsilon)^{1/4}z/\upsilon$

2.2. Turbulence model

The $k - \varepsilon$ turbulence model was employed for eddy viscosity. It consists of transport equations for the turbulent kinetic energy k and the turbulent dissipation ε. For low Reynolds number flow, the NTM model (Sana et al., 2007) with damping function of standard $k - \varepsilon$ model was employed, which implies that the model is applicable over the entire cross-stream dimension including the low Reynolds number region (viscous sublayer).

$$\frac{\partial k}{\partial t} + u\frac{\partial k}{\partial x} + w\frac{\partial k}{\partial z} = \frac{\partial}{\partial z}\left\{\left(\upsilon + \frac{\upsilon_t}{\sigma_k}\right)\frac{\partial k}{\partial z}\right\} + \upsilon_t\left(\frac{\partial u}{\partial z}\right)^2 - \varepsilon - B_k \tag{4}$$

$$\frac{\partial \varepsilon}{\partial t} + u\frac{\partial \varepsilon}{\partial x} + w\frac{\partial \varepsilon}{\partial z} = \frac{\partial}{\partial z}\left\{\left(\upsilon + \frac{\upsilon_t}{\sigma_\varepsilon}\right)\frac{\partial \varepsilon}{\partial z}\right\} + c_{1\varepsilon}f_1\frac{\varepsilon}{k}\upsilon_t\left(\frac{\partial u}{\partial z}\right)^2 - c_{2\varepsilon}f_2\frac{\varepsilon^2}{k}$$
$$- \frac{\varepsilon}{k}c_{3\varepsilon}B_k \tag{5}$$

Here k is the turbulent kinetic energy, ε is the dissipation rate, $\upsilon_t = c_\mu f_\mu k^2/\varepsilon$ is the eddy viscosity, $c_\mu = 0.09$ is a coefficient, f_μ is a coefficient as listed in Table 1, σ_k and σ_ε are turbulent Prandtl-Schmidt numbers for k and ε, respectively; B_k is the buoyancy flux and $c_{3\varepsilon}$ is coefficient, which are related to stratification effects and will be discussed in section 2.4.3.

The various coefficients in the standard $k - \varepsilon$ model and NTM model are summarized in Table 1.

2.3. Approaches for flow simulation

2.3.1. Driving forces
Driving forces are pressures outside the BBL. For current-only,

$$-\frac{1}{\rho}\frac{\partial \overline{p}}{\partial x} = -\frac{\partial}{\partial x}g\zeta = gJ \tag{6}$$

where ζ is the water level and J is the mean water surface slope.

For waves-only, the unsteady horizontal pressure gradient is determined in advance from a given horizontal free stream velocity $\tilde{u}_\infty$:

$$-\frac{1}{\rho}\frac{\partial \tilde{p}}{\partial x} = \frac{\partial \tilde{u}_\infty}{\partial t} + \tilde{u}_\infty\frac{\partial \tilde{u}_\infty}{\partial x} \tag{7}$$

Thus, for the wave-current cases, the driving force is described as:

$$-\frac{1}{\rho}\frac{\partial p}{\partial x} = -\frac{1}{\rho}\frac{\partial \overline{p}}{\partial x} - \frac{1}{\rho}\frac{\partial \tilde{p}}{\partial x} = gJ + \frac{\partial \tilde{u}_\infty}{\partial t} + \tilde{u}_\infty\frac{\partial \tilde{u}_\infty}{\partial x} \tag{8}$$

In the governing equations, the Stokes drift is not included as this model is mainly for the BBL, while the Stokes drift mainly affects the velocity near the surface.

2.3.2. Simplification of the advection term (1DV-approach)
In order to simplify the mathematical solution to the equations of momentum, continuity and $k - \varepsilon$ model, the relation $\frac{\partial}{\partial x} = -\frac{1}{c_e}\frac{\partial}{\partial t}$ was applied, where c_e is the wave celerity, x is the horizontal direction and t is the time. Previous work dealing with steady streaming within the ocean BBLs (Trowbridge and Madsen, 1984b; Hsu and Ou, 1994;

Deigaard et al., 1999; Holmedal and Myrhaug, 2009) have considered boundary layer models where the horizontal gradient operator in the convective term was approximated by this relation. This approximation reduces the two-dimensional boundary layer equations to spatial one-dimensional equations. This kind of boundary layer approximation can only be used in such conditions where the generation of time-dependent turbulence is confined to a relatively thin layer by the short period of the horizontal oscillation compared with the wavelength. More discussions have been presented by Henderson et al. (2004) and Kranenburg et al. (2012).

Using the continuity equation, the vertical velocity at level z can be expressed as:

$$w(z) = \frac{1}{c_e} \int_0^z \frac{\partial \tilde{u}}{\partial t} dz \tag{9}$$

where $\tilde{u}$ is oscillatory component of velocity $w = 0$ at $z = z_0$ is utilized.

2.4. Approaches for sediment simulation

2.4.1. Settling velocity and hindered settling effects

van Rijn's formula (van Rijn, 1993) was employed for the settling velocity $w_{s,0}$ in clear water,

$$w_{s,0} = \begin{cases} \frac{(s-1)gd_s^2}{18\upsilon} & 1 < d_s \leq 100\mu m \\ \frac{10\upsilon}{d_s}\left[\left(1 + \frac{0.01(s-1)gd_s^3}{\upsilon^2}\right)^{0.5} - 1\right] & 100 < d_s < 1000\mu m \end{cases} \tag{10}$$

in which d_s = sieve diameter.

The suspended sediment d_s generally is somewhat smaller than that of the bed depending on the composition of the bed and the strength of the flow dynamics. van Rijn (2007b)'s formula was employed to estimate the suspended sediment size,

$$d_s = \begin{cases} [1 + 0.006(d_{50}/d_{10} - 1)(\psi & for \quad \psi < 550 \quad and \quad d_{50} > d_{silt} \\ \quad - 550)]d_{50} \\ d_{50} & for \quad \psi \geq 550 \quad and \quad d_{50} > d_{silt} \\ d_{50} & for \quad d_{50} < d_{silt} \\ 0.5d_{silt} & for \quad d_{50} < 0.5d_{silt} \end{cases} \tag{11}$$

where $\psi = \frac{u_{wc}^2}{(s-1)gd_{50}}$ = mobility parameter. According to van Rijn (2007b)'s definition, $u_{wc}^2 = u_m^2 + u_c^2$, u_m = the peak orbital velocity near the bed, u_c = the depth-averaged current velocity, and $d_{silt} = 32$ μm. The lower limit is set to $d_{s\,min} = 0.5(d_{50} + d_{10})$.

Experiments have shown that the settling velocity is significantly reduced when the sediment concentration is high, which is the so-called hindered settling effect. For silt and sand, the hindered settling is slightly different, since the fluid movement around particles with $d < 100$ μm is laminar, and the fluid movement around settling particles with $d > 100$ μm is turbulent (Te Slaa et al., 2015). Silt and fine sand particles settle in the Stokes regime, and their geometry does not influence the hindered settling.

For sediment with grain size $d > 100\mu m$, according to Richardson and Zaki (1954) and van Rijn (1993), the settling velocity in a fluid-sediment suspension can be determined as:

$$w_s = w_{s,0}(1 - c_v)^n \tag{12}$$

where w_s = the particle fall velocity, c_v = the volume sediment concentration of solids, and n is the exponent, varying from 4.6 to 2.3. The influence of the particle size on the hindered settling of sand is given by Baldock et al. (2004) $n = 4.4(d_{50,ref}/d_{50})^{0.2}$, where $d_{50,ref}$ = 200 μm.

A more generic hindered settling formula for silt and very fine sand ($4\mu m \leq d \leq 100\mu m$) was derived by Te Slaa et al. (2015):

$$w_s = w_{s,0}\frac{(1 - c_v/\phi_{s,struct})^m(1 - c_v)}{(1 - c_v/\phi_{s,max})^{-2.5\phi_{s,max}}} \tag{13}$$

where $\phi_{s,struct}$ = 0.5 is the structural density, i.e., the solid content upon reaching the structural density of the bed, and $\phi_{s,max}$ = 0.65 is the maximum density, i.e., the solid content at the maximum packing of the particles. Upon reaching the structural density, a network of particles is formed and the settling velocities reduce to zero. The coefficient m represents the effects of the return flow and 1 was adopted in the verification cases.

2.4.2. Sediment simulation related to bed forms

Ripples exhibiting the formation of fluid vortices (orbital excursion larger than ripple length) are called vortex ripples (Bagnold, 1946). Hooshmand et al. (2015) suggested that for a silt-dominated sediment, $Re_\Delta = 450$ (Stokes Reynolds number) is the critical condition between ripple dominated bed and non-rippled bed. Sheet flow is present under stronger flow dynamics. Above plane beds, momentum transfer occurs primarily by turbulent diffusion, while above rippled beds, momentum transfer and the associated sediment dynamics in the near-bed layer are dominated by coherent motions, especially the process of vortex formation above the ripple lee slopes and the shedding of these vortices at times of flow reversal (van der A, 2005).

2.4.2.1. Sheet flow condition or 'flat bed'.
The term 'flat bed' is used in this paper to refer to 'dynamically plane' rough beds, including sheet flow conditions and rippled beds of mild steepness (< 0.12) (Davies and Villaret, 2002), above which momentum transfer occurs via turbulent processes rather than vortices. Under these conditions, the normal k- ε turbulence model is solved, and the stratification effects are included.

The flow under sheet flow conditions is affected by the relatively thin sheet flow layer with high sediment concentration, i.e., the mobile bed effects (Nielsen, 1992). The enhanced roughness due to mobile bed effects has been studied by many scholars (e.g., Wilson, 1989; Dohmen Janssen et al., 2001; Camenen et al., 2009). Camenen et al. (2009) proposed the Nikuradse's equivalent roughness by compiling many datasets,

$$\frac{k_s}{d_{50}} = 0.6 + 2.4\left(\frac{\theta}{\theta_{cr,ur}}\right)^{1.7} \tag{14}$$

in which θ is the Shields parameter, and $\theta_{cr,ur} = 0.115\frac{F_{rw}^{1.2}}{W_{s*}^{0.4}(s-1)^{0.3}}$ is the critical Shields parameter for the inception of the upper regime. $F_{rw} = \frac{u_w}{\sqrt{g\delta}}$ is the wave Froude number, where u_w is the wave orbital velocity, $\delta = \sqrt{\upsilon T}$ is the thickness of the viscous (Stokes) layer, and T is the wave period. $W_{s*} = \left[\frac{(s-1)^2}{(g\upsilon)}\right]^{1/3} w_s$ is the dimensionless settling velocity. If $\theta < \theta_{cr,ur}$, then $k_s < 3d_{50}$, which corresponds approximately to the skin friction. For finer sediments, the grain roughness becomes smaller and the enhanced roughness from mobile bed effects becomes more important.

2.4.2.2. Rippled bed.
In a near-bed layer of approximately two ripple heights above the rippled bed, the flow dynamics are dominated by coherent periodic vortex structures, whereas above this layer the coherent motions break down and are replaced by random turbulence (Davies and Villaret, 1999). This leads to sediment in suspension having considerably greater heights compared to flat beds. Ripple vortices are 3D or 2DV phenomena, and it is not physically justifiable to describe hydrodynamics and sediment dynamics over ripples with a 1DV approach. However, from a practical point of view, more sophisticated 2DV models are unduly complex and, therefore, 1DV models are preferred (van Der Werf, 2003). Recent research has proved the merits of the 1DV approach (Davies and Thorne, 2005; van der A, 2005; van der Werf et al., 2006). In the following sections, some key

approaches are introduced regarding ripple prediction, roughness, vortex eddy viscosity and pick-up function.

(1) Ripple prediction

There are many formulas for predicting ripple parameters (e.g., Nielsen, 1992; Mogridge et al., 1994; Khelifa and Ouellet, 2000). Khelifa and Ouellet (2000)'s method was employed in this study, which has been verified by many experimental and field data and can be used for both wave-only and combined wave-current conditions.

$$\frac{2\lambda}{d_{wc}} = 1.9 + 0.08 \ln^2(1 + \psi_{wck}) - 0.74 \ln(1 + \psi_{wck}) \tag{15}$$

$$\frac{2\eta}{d_{wc}} = 0.32 + 0.017 \ln^2(1 + \psi_{wck}) - 0.142 \ln(1 + \psi_{wck}) \tag{16}$$

where η is the ripple height and λ is the ripple length. $d_{wc} = TU_{wc}$, $\psi_{wck} = \frac{U_{wc}^2}{(s-1)gd}$, $U_{wc} = \sqrt{\left(\frac{u_m}{\pi}\right)^2 + \overline{u}_c^2 + 2\frac{u_m \overline{u}_c}{\pi}|\cos\phi|}$, T = wave period, $\overline{u}_c$ = depth-averaged current velocity, u_m = wave orbital velocity and ϕ = the angle between wave and current. Under wave and wave-current motions, the applicability of the formula has been tested for ψ_{wck} varying in the ranges of 0.3–20 and 0.7–145, respectively.

(2) Bed form roughness

The bed form roughness is determined empirically from ripple parameters

$$k_s = a_s \frac{\eta^2}{\lambda} \tag{17}$$

where a_s is a constant. The factor a_s is still arguable, such as 8 (Nielsen, 1992), 25 (Davies and Thorne, 2005) and 27.7 (Grant and Madsen, 1982). Nielsen (1992) also suggested the roughness contribution from the moving sediment over ripples.

(3) Eddy viscosity and diffusion coefficient

In accordance with the physical background, a two-layer model was adopted, i.e., the vortex-dominated layer at the bottom and the turbulence-dominated layer above, separated by twice the ripple height (Davies and Thorne, 2005; van der Werf et al., 2006).

In the vortex-dominated layer, the mean eddy viscosity adopts Nielsen (1992)'s height-invariant expression for very rough beds,

$$\overline{v_{tN}} = c_v A \omega k_s \tag{18}$$

in which $c_v = 0.004$–0.005.

The time varying eddy viscosity is assumed to be given by the real part of the following expression (Davies and Thorne, 2005)

$$v_{tN}(t) = \overline{v_{tN}} f(\omega t) \tag{19}$$

with $f(\omega t) = (1 + \varepsilon_0 + \varepsilon_1 e^{i\omega t} + \varepsilon_2 e^{2i\omega t})$. $f(\omega t)$ is briefly introduced in Appendix B. Please see Davies and Thorne (2005) for more details. In the turbulence-dominated layer, the k-ε model was employed to provide the eddy viscosity. At the interface between the vortex-dominated layer and the turbulence-dominated layer, the values of k and ε were derived from the mixing length $l = 2\kappa\eta$ (Davies and Thorne, 2005) by $\varepsilon = c_\mu \frac{k^{3/2}}{l}$. Thus, at the edge of vortex layer,

$$k_{vortex}(t) = \left[\frac{v_{tN}(t)}{0.8\eta}\right]^2,$$
$$\varepsilon_{vortex}(t) = c_\mu \frac{v_{tN}(t)^3}{(0.8\eta)^4} \tag{20}$$

Then above the vortex layer, the model reverts to the standard turbulence closure scheme.

The sediment diffusivity in the lower layer above rippled beds is significantly larger than the eddy viscosity, with $\varepsilon_s(t) = \beta \frac{v_t(t)}{\sigma}$

(Nielsen, 1992; Thorne et al., 2002). The value of the parameter has been assumed to revert smoothly from its value of $\beta = 4.0$ in the lower vortex layer towards unity in the upper layer, according to the power law rule:

$$\beta = 4.0 - 3.0\left(\frac{z - 2\eta}{h - 2\eta}\right)^\gamma \tag{21}$$

Where h is the water depth, z is the elevation from the bottom and the coefficient γ = 0.4–1.

(4) Time-process of the reference concentration over rippled bed

The time-varying reference concentration is (Davies and Thorne, 2005)

$$c_a(t) = \overline{c_a} \frac{0.5((1 + \varepsilon_0) + \varepsilon_1 e^{iwt} + \varepsilon_2 e^{2iwt})((1 + a_c e^{2iwt}) + c.c)}{((1 + \varepsilon_0) + 0.25 A_c |\varepsilon_0|(e^{i(2\phi_1 - 2\phi_c)} + c.c))} \tag{22}$$

in which $\overline{c_a}$ is the mean reference sediment concentration. For more details, please see Appendix B and Davies and Thorne (2005).

2.4.3. Stratification effects

When sediment is suspended, the vertical gradient of sediment concentration causes the vertical gradient of density to increase. Studies reported in literatures show an appreciable effect of suspended sediment on the turbulence properties (Traykovski et al., 2007; Winterwerp, 1999). If the sediment concentration gradient is high, sediment-induced turbulence damping can largely affect the velocity profile and the transport rate, especially for fine sediment (Conley et al., 2008; Hassan and Ribberink, 2010; Kranenburg et al., 2013; Winterwerp, 2001). Thus, the sediment-induced turbulence damping is an important term for high concentration layer modelling. Some models consider sediment-flow interaction processes in different ways (Hassan and Ribberink, 2010; Kranenburg et al., 2013). Generally, the buoyancy flux B_k accounts for the conversion of turbulent kinetic energy to mean potential energy with the mixing of sediment, which is considered equivalent to buoyancy flux in a salt-stratified or thermally stratified flow. The following expressions are used to describe the buoyancy flux B_k and the Brunt-Vaisala frequency N,

$$B_k = \frac{v_t}{\sigma_v} N^2; \quad N^2 = -\frac{g}{\rho_m} \frac{\partial \rho_m}{\partial z} \tag{23}$$

The coefficient in Eq. (5) $c_{3\varepsilon} = 0 \quad N^2 > 0$ and $c_{3\varepsilon} = 1 \quad N^2 < 0$. ρ_m is the density of the local water-sediment mixture,

$$\rho_m = \rho_w + (\rho_s - \rho_w)c_v \tag{24}$$

in which ρ_w is the density of clear water, ρ_s is the sediment particle density, and c_v is the volumetric sediment concentration.

To evaluate the damping of vortex viscosity, van Rijn (2007b)'s formula for damping effect was employed by a damping coefficient ϕ_d,

$$v_{tN}(t) = \phi_d v_{tN}(t) \tag{25}$$

in which $\phi_d = \phi_{fs}[1 + (c/c_{gel,s})^{0.8} - 2(c/c_{gel,s})^{0.4}]$, $\phi_{fs} = d_{50}/(1.5d_{sand})$, and $\phi_{fs} = 1$ for $d_{50} \geq 1.5d_{sand}$. $c_{gel,s} = 0.65$ = maximum bed concentration in volume.

2.4.4. Reference concentration

(1) Approaches for reference concentration

The reference concentration considering silt was employed (Yao et al., 2015).

$$c_a = \beta_y (1 - p_{clay}) f_{silt} \frac{d_{50}}{z_a} \frac{T^{1.5}}{d_*^{0.3}} \tag{26}$$

in which, $\beta_y = 0.015$ is an original empirical coefficient for sand, and Yao et al. (2015) extended it to silt by using $\beta_y = 0.118 d_*$, with a

maximum value of 0.118 and minimum value of 0.015; $f_{silt} = \frac{d_{sand}}{d_{50}}$ is the silt factor ($f_{silt} = 1$ for $d_{50} > d_{sand}$), and $d_{sand} = 62\,\mu m$; p_{clay} is the percentage of clay material in the bed; $d_* = d_{50}[(s-1)g/\upsilon^2]^{1/3}$ is the dimensionless particle size; $T = \frac{(\tau' - \tau_c)}{\tau_c}$, in which τ' is originally the time-averaged effective bed-shear stress under currents and waves; τ_{cr} is the critical bed shear stress. The reference height za is defined as the maximum value of half the wave-related and half the current-related bed roughness values $k_{s,c,r}$, with a minimum value of 0.01 m.

For sand simulation in sheet flow condition and rippled beds, Zyserman and Fredsøe (1994)'s formula and Nielsen (1992)'s formula were recommended respectively.

Zyserman and Fredsøe (1994)'s formula:

$$c_a = \frac{0.331(\theta - \theta_c)^{1.75}}{1 + 0.720(\theta - \theta_c)^{1.75}},$$
$$at\ z_a = 2d_{50} \tag{27}$$

in which θ is the instantaneous Shields number and θ_c is the critical Shields number.

Nielsen (1992)'s formula:

$$\bar{c}_a = 0.0022\theta_r^3,$$
$$at\ z_a = 2d_{50} \tag{28}$$

in which θ_r is the ripple-adjusted value of Shields number.

When applying the formulas of the reference concentration in oscillatory flows, a zero value for the bed concentration is unrealistically obtained during the stage of a wave cycle, when the shear stress is lower than the critical value (Fredsøe and Deigaard, 1992). To overcome this shortcoming, the deposited sediment from the last time step was considered here. At the reference level, from the governing equation, the diffusion is ignored: $\frac{\partial c}{\partial t} - w_s \frac{\partial c}{\partial z} = 0$.

$$c_a^n = c_a^{n-1} + w_s \frac{\Delta t}{\Delta z}(c_{za+1}^{n-1} - c_a^{n-1}) \tag{29}$$

Then, $c_a(t) = \max(c_a^n, c_a(t))$, in which, c_a^n is the reference sediment concentration at the present time step, c_{za+1}^{n-1} is the c at the grid above the reference height z_a at the last time step, and c_a^{n-1} is the reference sediment concentration at the last time step. Fig. 3 shows the comparison of the non-adjusted and adjusted reference sediment concentration.

(2) Critical shear stress of sediment incipience

In the above formulas, the critical shear stress needs to be determined and generally the Shields curve can be employed. However, due to the dual features (both non-cohesive and cohesive behavior) of silty sediments, the Shields curve which is normally used for non-cohesive sediments cannot be used for silt. A general expression of silt-sand incipience motion was employed here, which considered the cohesive force and additional static water pressure for fine sediment (Zuo et al., 2017).
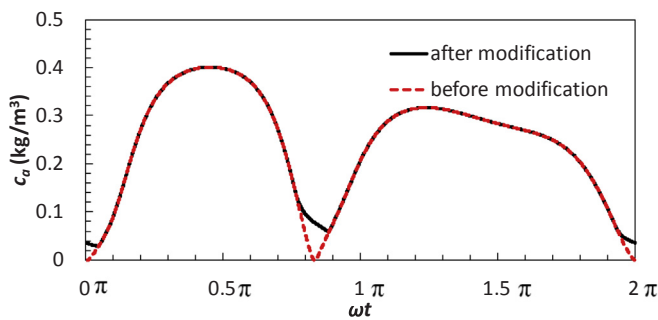
Fig. 3. Comparison of reference concentration at the reference height and the revised version (in case of the experiment conditions of O'Donoghue and Wright (2004)) (the black line represents the revised reference concentration and the red dash line represents the original reference concentration).

$$\theta_{zc} = \begin{cases} 0.025\,\mathrm{Re}\,d_*^{-0.07} & \mathrm{Re}\,d_* < 1 \\ 0.00543\ln(\mathrm{Re}\,d_*) + 0.025 & 1 \le \mathrm{Re}\,d_* \le 100 \\ 0.05 & \mathrm{Re}\,d_* > 100 \end{cases} \tag{30}$$

where $\theta_{zc} = \frac{\tau_c}{\rho_w(s-1)gd + a\beta_c\rho_w\frac{\varepsilon_k + gh\delta_s\sqrt{\delta_s/d}}{d}}$; $\mathrm{Re}\,d_* = \frac{d}{4\upsilon}\sqrt{(s-1)gd}$ is the non-dimensional sand Reynolds number; τ_c is the critical shear stress; $\varepsilon_k = 1.75 \times 10^{-6}\,m^3/s^2$ is the cohesive force coefficient; $\delta_s = 2.31 \times 10^{-7}\,m$ is the bound water thickness; $a = 0.19$ is a coefficient, and β_c is the compaction coefficient, normally $\beta_c = 1$ for well-compacted sediments.

2.5. Boundary conditions and initial conditions

At the bottom: $u(z_0, t) = 0$, $w(z_0, t) = 0$ $z_0 = k_s/30$

$$k(z_0, t) = \upsilon_t \left|\frac{\partial u}{\partial z}\right|/\sqrt{c_1},$$

$$\varepsilon(z_0, t) = (c_1)^{3/4}\frac{k^{3/2}}{\kappa z_0},$$

$$\varepsilon_s \frac{\partial c}{\partial z} = -\omega_s c_a,$$
$$at\ z = z_a$$

At the upper boundary: For waves alone, the upper edge of the flow domain, $z = z_{max}$ is chosen where the boundary layer effects have disappeared. The condition of no shear is applied at the edge of the bottom boundary layer at $z = z_{max}$. The Neumann condition is applied on the velocity, $\frac{\partial}{\partial z}u(z_{max}, t) = 0$.

Zero flux conditions are imposed for the turbulent quantities at the edge of the flow domain, $\frac{\partial k}{\partial z} = \frac{\partial \varepsilon}{\partial z} = 0$.

For wave-current conditions, the velocity at z_{max} (upper boundary) is given by the Dirichlet condition

$$u(z_{max}, t) = \bar{u} + \tilde{u}_\infty(t)$$

in which $\bar{u}$ is the mean flow velocity, and $\tilde{u}_\infty(t)$ is the wave orbital free stream velocity.

A zero flux condition is imposed on the sediment concentration at the upper boundary:

$$(\omega_s - w)c + \varepsilon_s \frac{\partial c}{\partial z} = 0,$$
$$at\ z = z_{max}$$

2.6. Numerical discretization

Geometric stretching of the mesh was applied to obtain a fine resolution close to the bed (Zhang et al., 2011a,b), and a stretching factor of 1.05 was applied. Our experience shows that the grid structure with 50–100 vertical grid cells is sufficient for resolving the boundary layer.

The FVM (finite volume method) method was employed to discretize the governing equations. Time discretization is based on the θ_f method. A coefficient θ_f was employed. When $\theta_f = 0$, the discretization scheme is explicit; when $\theta_f = 1$, it is an implicit scheme; and when $\theta_f = 0.5$, it is a Crank-Nicholson semi-implicit scheme. In this study, the implicit scheme was employed. The convection term was discretized by a first-order upwind scheme. After discretization, tridiagonal matrices were obtained, and the TDMA method (tridiagonal matrix algorithm) was employed to solve the matrices.

The convergence condition was settled as 10^{-5} for the $u, \upsilon_t, k, \varepsilon$ and c at the same phase between the two periods, i.e., the maximum differences of every variable should be less than 10^{-5}. As the scheme is implicit, it is less sensitive to the Courant number (CFL) for convergence and larger values of CFL can be tolerated, with $CFL = \Delta t/\Delta z\sqrt{gh}$, in which Δt is the time step and Δz is the grid length interval. For a better practice performance, the maximum of CFL is less than 10 during the following simulations. The time step (for example 4000–10,000 sections of the wave period) and space step are both very small to simulate
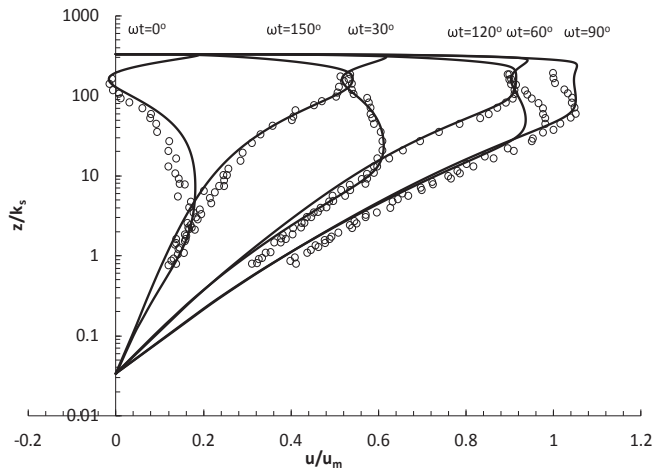
Fig. 4. Comparison of calculated and measured wave velocity profiles (Jensen et al. (1989)'s experiment, dots were measured, lines were calculated and ω is the angular frequency).

the BBL, as the thickness of BBL is only in the order of centimeters or even millimeters. Furthermore, tests show that, the approach of Eq. (29) does not impact the numerical convergence.

3. Model verification

3.1. Flow simulation in wave-current BBL

Experimental data of Jensen et al. (1989), Klopman (1994), Umeyama (2005) and Fredsøe et al. (1999) were used to verify the model. The former three experimental cases are over flat bed and the last one is over rippled bed.

Figs. 4–7 show the verification of Jensen et al. (1989)'s experiment data (Test 13). The experiments were carried out in a U-shaped oscillatory-flow water tunnel. The velocity amplitude was 2 m/s and the wave period was 9.72 s. A sheet of sandpaper was glued at the bottom with a sand-roughness value of $k_s = 0.84$ mm. The oscillatory flow in the tunnel was driven by an electronically controlled pneumatic system, and the velocity was sinusoidal. For more details, please refer to Jensen et al. (1989). According to Tanaka and Thu (1994), the laminar wave boundary was defined as Reynolds number $\text{Re}_{wave} = Au_m/v$ less than 1.8×10^5. The wave Reynolds number in this case was 61.9×10^5, which indicates that it was a turbulent wave boundary layer and the
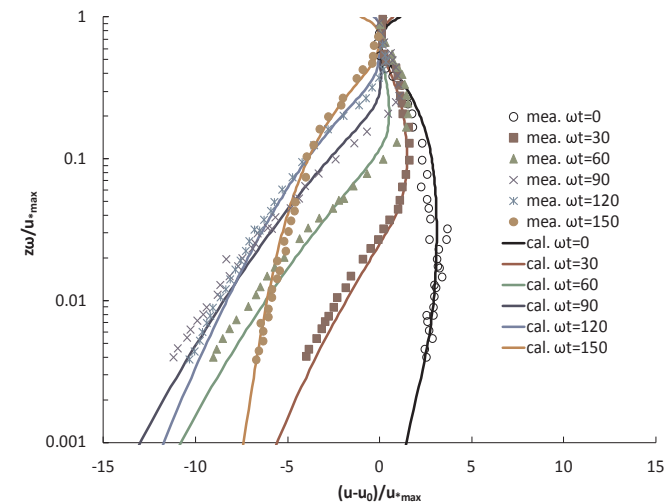
Fig. 5. Verification of velocity defect of test 13 of Jensen et al. (1989)'s experiment.
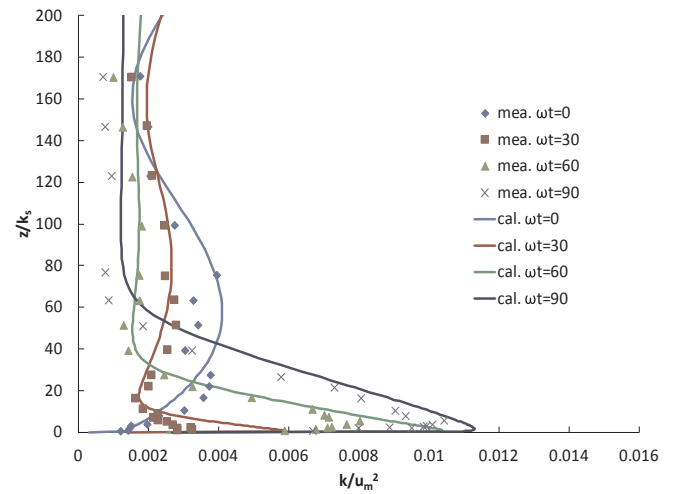
Fig. 6. Verification of kinetic energy distribution of test 13 of Jensen et al. (1989)'s experiment.
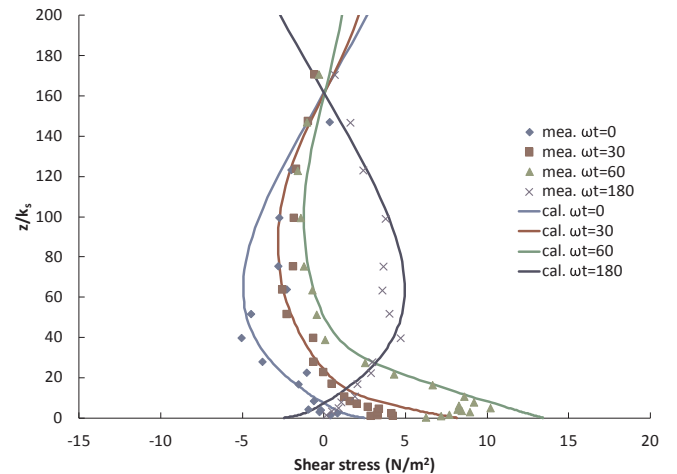
Fig. 7. Verification of shear stress distribution of test 13 of Jensen et al. (1989)'s experiment.

standard k-ε model was adopted here. The simulated velocity distribution in different phases matched the measured data well. The simulated velocity defect, kinetic energy, shear stress and shear velocity matched the measured data.

Fig. 8 and Fig. 9 show the velocity amplitude, the mean velocity distribution under the wave-only condition and the combined wave-current condition in Klopman (1994)'s experiment. The wave height was 0.12 m, wave period was 1.4 s and k_s was 0.84 mm. The mean current velocity was 0.16 m/s and water depth was 0.5 m. It can be seen that the model simulated the velocity distribution well. In this case, the wave Reynolds number is 5.9×10^3, which means that it is a laminar wave boundary layer. The NTM turbulence model could get a better result, while the standard k-ε turbulence model overestimated the BBL (Fig. 8). In the wave bottom boundary layer, beyond the log-distribution layer, there was an over-shoot at the edge of the BBL. The wave-induced current was positive near the bottom and negative above the boundary layer. For the wave following current, the velocity near the bottom mainly increased compared with the current-only case, while for the wave opposing current, the velocity near the bottom decreased. At the upper part, the velocity changes showed a different tendency related to Stokes drift effects, which is not shown in this paper.

Umeyama (2005) carried out experiments to study changes in the mean velocity profile owing to the interaction between waves and currents in a recirculating wave tank. The wave tank is 25 m long, 0.7 m
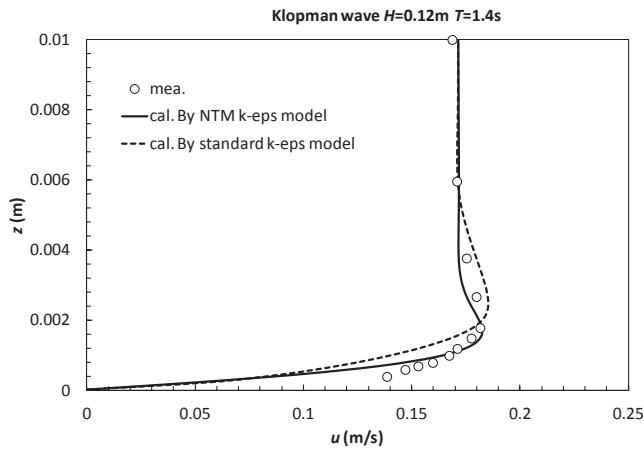
Fig. 8. Comparison of calculated and measured velocity amplitude profile of wave-only case (Klopman (1994)'s experiment).

wide and 1.0 m deep. The experimental conditions are listed in Table 2. Fig. 10 shows the comparison of the measured and calculated phase-average velocity distribution for the wave-only case (W2, W4), wave following case (WCF2, WCF4) and wave opposing case (WCA2, WCA4). The results showed that the calculated mean velocity for different cases matched the measured data well.

Fredsøe et al. (1999) carried out experiments to study the combined wave and current boundary layer flow over a ripple-covered bed. The fixed ripples are 22 cm in length and 3.5 cm in height. The water depth measured from the ripple crest is 41.5 cm. The W1 case (wave-alone) and three combined wave-current tests (WC1-WC3) were employed to verify the model. The space-averaged maximum wave orbital velocity is 22.9 cm/s, and wave period is 2.5 s. The ratio of wave velocity to current velocity from WC1 to WC3 is 1.0, 1.7 and 2.4. The velocity near the

bed is affected by the ripples and show differences at different sections. Fredsøe et al. (1999) defined the space-averaged velocity as $u_{sp} = 1/\lambda \int_0^\lambda u(x)dx$ with λ is ripple length. Here the space-averaged velocity profiles are used. Fig. 11 shows the comparison of the measured and calculated velocity distribution at different phases for the wave-only case (W1). Fig. 12 shows the verification of the period-and-space-averaged velocity profiles for the wave-only case (W1) and wave following currents case (WC1, WC2 and WC3). The results showed that the agreement of the calculated and measured velocity profiles is acceptable, with RMSE (root-mean-square error) = 0.008, 0.011, 0.009 and 0.009 for W1, WC1, WC2 and WC3, respectively. The flow movement over ripples is three-dimensional; though there is discrepancy at some phases, the simplified 1DV model still can simulate the space-mean flow.

Based on the validation, it can be concluded that the model is able to simulate the flow dynamics near the bed bottom in wave-current conditions. It is able to simulate the mean velocity distribution, velocity amplitude, Reynolds stress, eddy viscosity, turbulence and phase defect within the wave period. This model has been implemented and validated not only for the full turbulence case, but also for low-Reynolds number cases. It can simulate the wave-induced net current and the combined wave-current interaction. All these processes are important for sediment transport in the BBL, which means that this model can provide suitable flow dynamics for sediment simulation. However, this model is still not able to simulate the velocity distribution near the surface as the Stokes drift is not taken into account. This is acceptable for the purpose of studying the high sediment concentration near the bottom.

3.2. Verification of sediment movement in the wave-current BBL

Experimental data of silt and very fine sand carried out by Zhou and Ju (2007), Li (2014) and Yao et al. (2015) were used to verify the
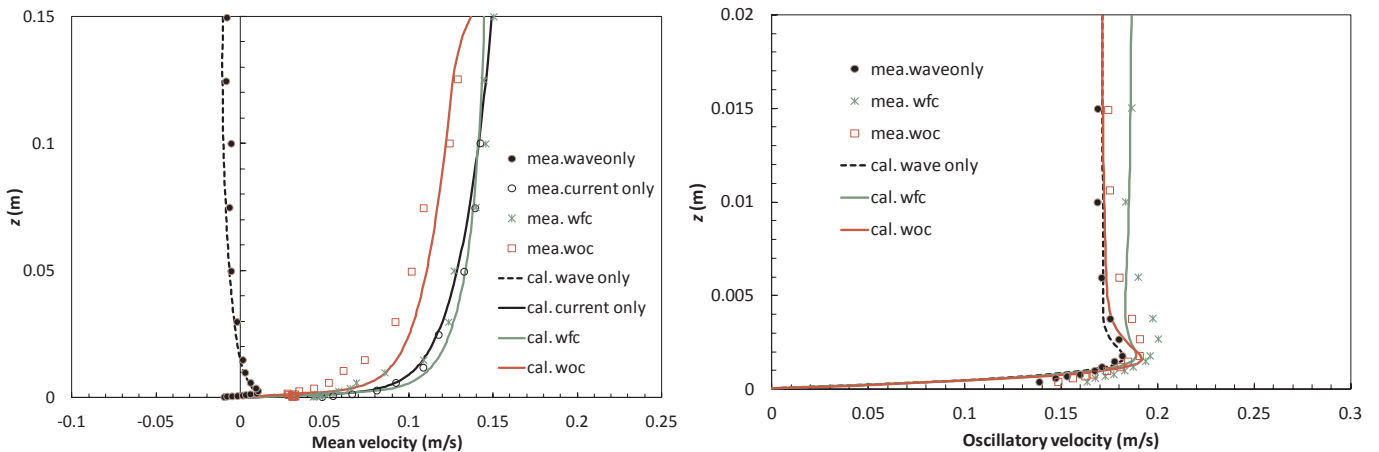
Fig. 9. Verification of profiles of the mean velocity (left) and oscillatory velocity (right) in Klopman (1994)'s experiment (wfc: wave following current; woc: wave opposing current).

Table 2
Experiment conditions of Umeyama (2005)'s experiment.

Case	h (m)	H (m)	T (s)	u_c (m/s)	$\bar{u}$ at z (m/s)	reference height z (m)	note
W2	0.2	0.0251	1.0	0	0	0.2	Wave only
W4	0.2	0.028	1.4	0	0	0.2	Wave only
WCF2	0.2	0.0231	1.0	0.12	0.111	0.05	Wave following current
WCF4	0.2	0.0250	1.4	0.12	0.117	0.05	Wave following current
WCA2	0.2	0.0215	1.0	−0.12	0.112	0.07	Wave opposing current
WCA4	0.2	0.0270	1.4	−0.12	0.118	0.07	Wave opposing current
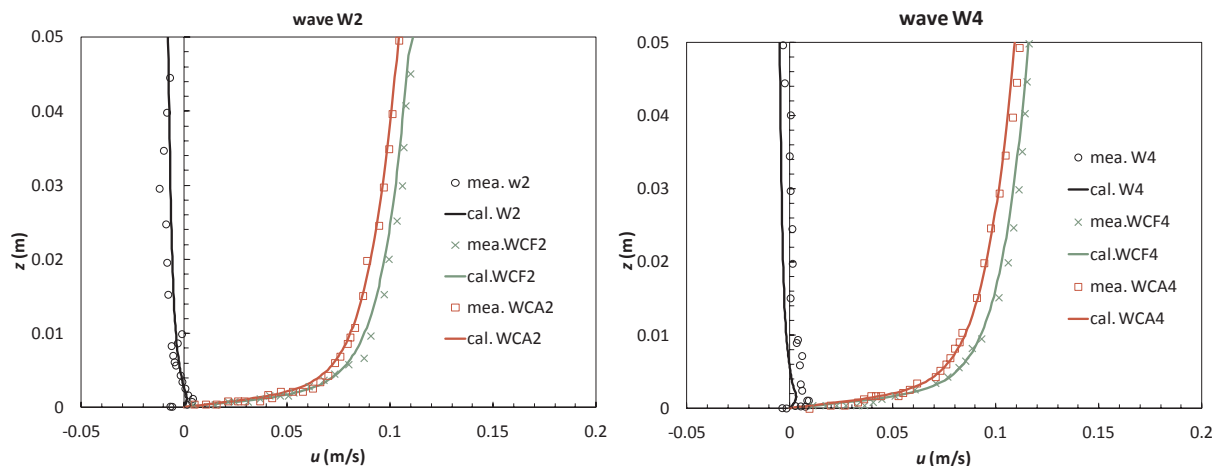
Fig. 10. Verification of mean velocity distribution of Umeyama (2005)'s experiment in case of wave-only (W2, W4), wave following current (WCF2, WCF4) and wave against current (WCA2, WCA4).
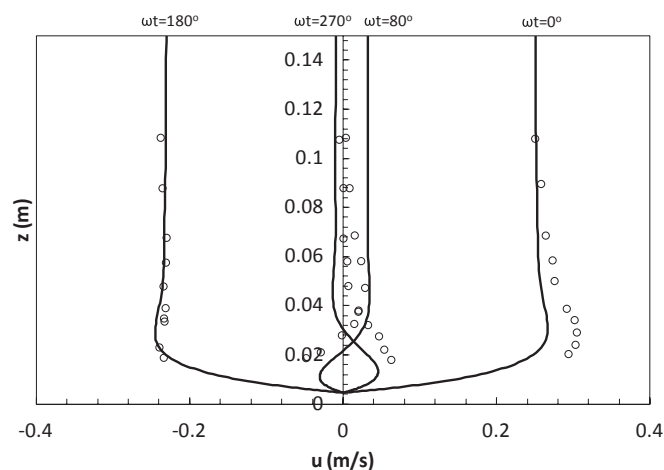
Fig. 11. Comparison of the measured and calculated velocity profiles at different phases for case W1. $\omega t = 0^o$ corresponds to the passage of the wave crest (lines were calculated and dots were measured).
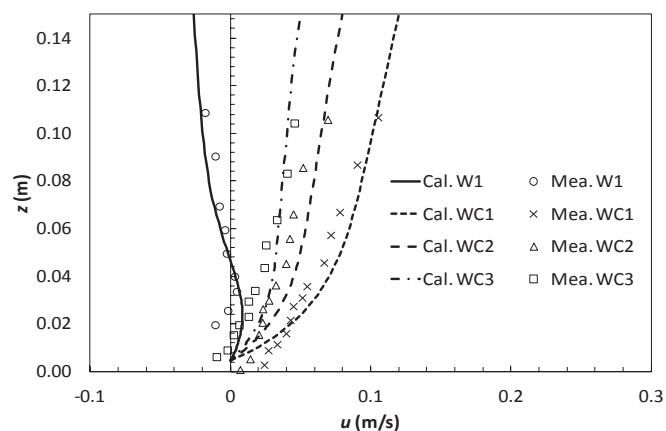
Fig. 12. Verification of the period-and-space-averaged velocity profiles for cases W1, WC1, WC2 and WC3.

model, as listed in Table 3. The bed forms in these three cases are ripples. Besides, in Yao et al. (2015)'s experiment on silt, the case of s1-f3212 and s1-o3812, ripples disappeared when currents were imposed, which could present an evidence of 'flat bed'. There were still few experiments on silty sediments under sheet flow conditions, thus we collected some experimental data on fine sand to verify the model, such

as O'Donoghue and Wright (2004) and Dohmen Janssen et al. (2001). The sediment materials in these two experiments include fine sand to coarse sand which can also show the difference of sediment concentration profiles. The flow dynamics conditions in the verification cases included wave only cases and combined wave-current cases.

3.2.1. Dohmen Janssen et al. (2001)'s case

Dohmen Janssen et al. (2001)'s experiments were carried out in the Large Oscillating Water Tunnel (LOWT) of Delft Hydraulics, in which near-bed orbital velocities in combination with a net current could be simulated at full scale. Three uniform sands with different mean grain sizes were used. The experimental conditions were listed in Table 4. Fig. 13 shows the comparison of the measured and calculated sediment concentration profiles. It can be concluded that, the model is able to simulate the mean concentration profiles for different grain sizes.

3.2.2. Case of O'Donoghue and Wright (2004)

O'Donoghue and Wright (2004) carried out experiments in an oscillatory tunnel under asymmetry oscillatory motion, which was described as $u_\infty(t) = U_1 \sin \omega t - U_2 \cos 2 \omega t$, with $U_1 = 1.2$ m/s and $U_2 = 0.3$ m/s, $T = 5$ s, see Fig. 14. The experimental sediments comprised three well-sorted sands, fine, medium and coarse sand with $d_{50} = 0.15$, 0.28 and 0.51 mm, $d_{10} = 0.10$, 0.17 and 0.36 mm, respectively.

Fig. 15 shows the comparison of the calculated and measured values of the mean sediment concentration profiles. The RMSEs (root-mean-square error) are 0.027, 0.022 and 0.025 for the cases of FA5010, MA5010 and CA5010, respectively. It can be concluded that, the model is able to simulate the sediment concentration profile changes as results of the sediment grain size changes. Fig. 16 and Fig. 17 show the sediment flux profiles in different phases during the intra-wave process. The calculated flux profiles in most phases were in agreement with the measured ones. As expected, the flux magnitudes were much larger in the case of the fine sand compared with the medium sand. This was due to the higher suspended concentrations in the case of fine sand.

Fig. 18 shows the comparison of the calculated and measured net flux profiles. Although deviations exist in the values, the model is able to simulate the changes of the flux direction for different grain particles, i.e., the flux of 'fine' sand (FA5010) shows offshore direction, while the fluxes of 'medium' and 'coarse' sands (MA5010 and CA5010) show onshore direction. However, in the case of fine sand, the calculated fluxes in the minus flow phase ($t/T = 0.42$–0.71 in case FA5010) were not as well simulated. Although the maximum offshore velocity was only approximately 60% of the maximum onshore velocity, the flux value in the phase of maximum offshore velocity ($t/T = 0.71$) was similar to

Table 3
Verification cases for sediment movement.

Case	Flow dynamics	Wave type	d_{50} (mm)	Bed form
Dohmen Janssen et al. (2001)	Wave + current	Wave flume	0.13–0.32	Sheet flow
O'Donoghue and Wright (2004)	Wave only	Oscillatory tunnel	0.15–0.51	Sheet flow
Zhou and Ju (2007)	Wave + current	Wave flume	0.062–0.11	Rippled bed
Li (2014)	Wave only	Wave flume	0.045–0.11	Rippled bed
Yao et al. (2015)	Wave and wave + current	Wave flume	0.046–0.088	Rippled bed & flat bed

Table 4
Experimental conditions of Dohmen Janssen et al. (2001).

Case	h (m)	u_m (m)	T (s)	u_c (m/s)	d_{50} (mm)	d_{10} (mm)
D1	0.8	1.47	7.2	0.24	0.13	0.10
D2	0.8	1.47	7.2	0.23	0.21	0.15
D3	0.8	1.47	7.2	0.26	0.32	0.22

that at the maximum onshore velocity ($t/T = 0.21$). This might have been caused by the unsteady effects that occurred in the case of fine sand (Dohmen-Janssen et al., 2002). As investigated during the experiment (O'Donoghue and Wright, 2004), at $t/T = 0.21$, the fine sand was carried high into the flow as a result of the high flow velocities, contributing to the high onshore flux in this phase. Because of its low settling velocity, the fine sand slowly settled, however, a significant proportion did not settle back to the bed as the flow velocity decreased. The high offshore flux during the offshore flow was therefore caused by the presence of the high concentrations resulting from the slow settling of sand entrained by the previous high onshore velocities.

3.2.3. Zhou and Ju (2007)'s experiment

Zhou and Ju (2007)'s experiment was carried out in a wave flume in Nanjing Hydraulic Research Institute. The flume is 175 m long, 1.2 m wide and 1.6 m deep. The experimental sediments are fine sediments with $d_{50} = 0.062$ mm, water depth $h = 50$ cm, wave period $T = 2$ s, wave height $H = 0.1$–0.2 m, and mean current velocity $u_c = 0.0$, 0.123, 0.188, 0.253, 0.319 m/s. Fig. 19 shows the measured and calculated sediment concentration profiles under wave-only and wave-current conditions. According to Khelifa and Ouellet (2000)'s formula, the ripple height is 0.5–0.7 cm and 1.0–1.2 cm, and the ripple length is 4.7–5.1 cm and 7.8–8.5 cm.
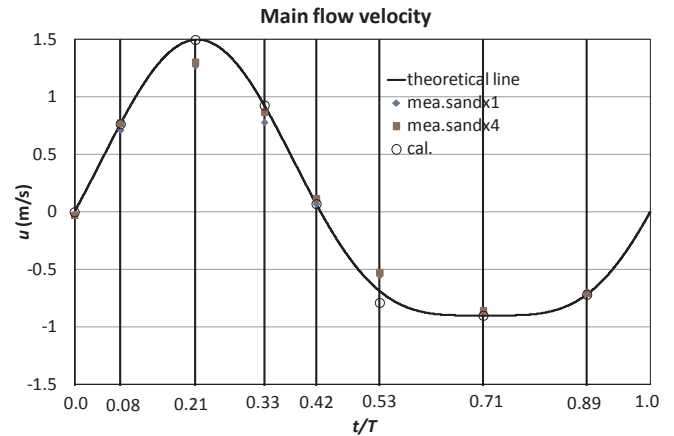
Fig. 14. Time series of the main flow velocity in O'Donoghue and Wright (2004)'s experiment.

Under the wave-only conditions, the measured sediment concentration profile can be considered as a fully developed equilibrium profile because of the relatively small net current. However, when the current is added, sufficient sediment source and a certain distance are needed to establish the equilibrium concentration. The length of sediment section in this experiment was only 10 m, and it was too short to develop the equilibrium concentration for combined wave-current conditions.

In steady flow conditions, the sediment transport along the distance can be described by the balance equation:

$$q\frac{dc}{dx} + g_{si} - g_{s0} = 0 \tag{31}$$
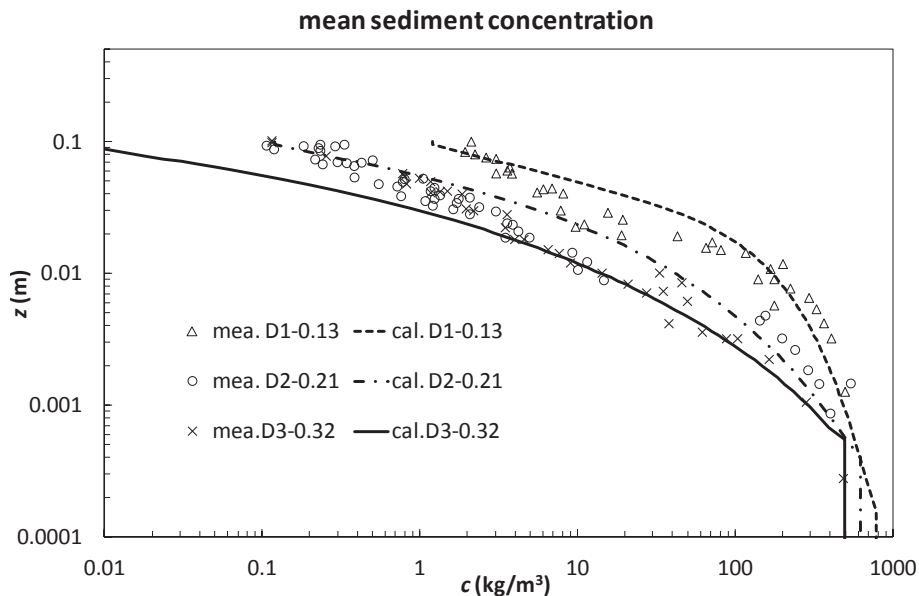
Fig. 13. Comparison of measured and calculated sediment concentration profiles of Dohmen Janssen et al. (2001).
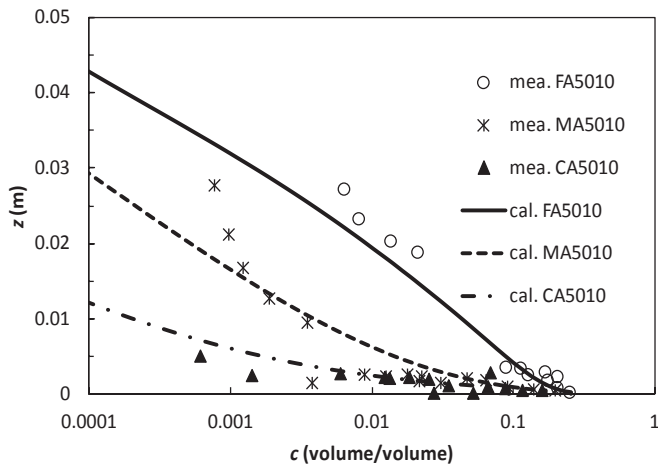
Fig. 15. Verification of mean sediment concentration profiles for different sand sediments of O'Donoghue and Wright (2004)'s experiment.

where $q = uh$ is the discharge per unit width, $g_{si} = \alpha c \omega_s$ is deposition sediment flux per unit time, and $g_{si} = \alpha c_* \omega_s$ is erosion flux per unit time entrained from the bed. α is coefficient of saturation recovery and $\alpha = 1$ is assumed here. c_* is equilibrium sediment concentration.

Substituting the deposition flux and erosion flux into the balance equation, and integrate above equation, we have

$$(c_0 - c_*)\exp\left(-\frac{\alpha\omega_s}{uh}x\right) = c - c_* \tag{32}$$

where c_0 is the sediment concentration at the input section. To obtain the equilibrium distance, let $c = c_*$, then

$$(c_0 - c_*)\exp\left(-\frac{\alpha\omega_s}{uh}x\right) = 0 \tag{33}$$

During experiment, the input sediment concentration $c_0 = 0$; it needs $\exp\left(-\frac{\alpha\omega_s}{uh}x\right) \approx 0$, which means $-\frac{\alpha\omega_s}{uh}x$ has to be a very small number. In practice, if we assume that $c/c_* = 99\%$ is enough for the equilibrium, then
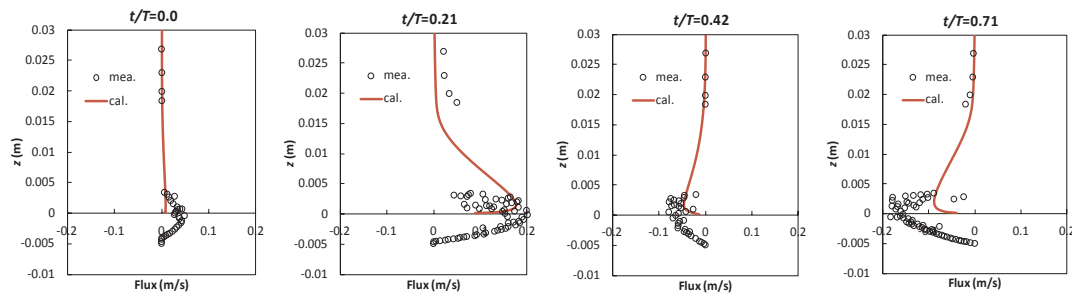
Fig. 16. Verification of flux profiles at selected phases for experiment FA5010 (values below 0 are in sheet flow layer which are not included in the model).
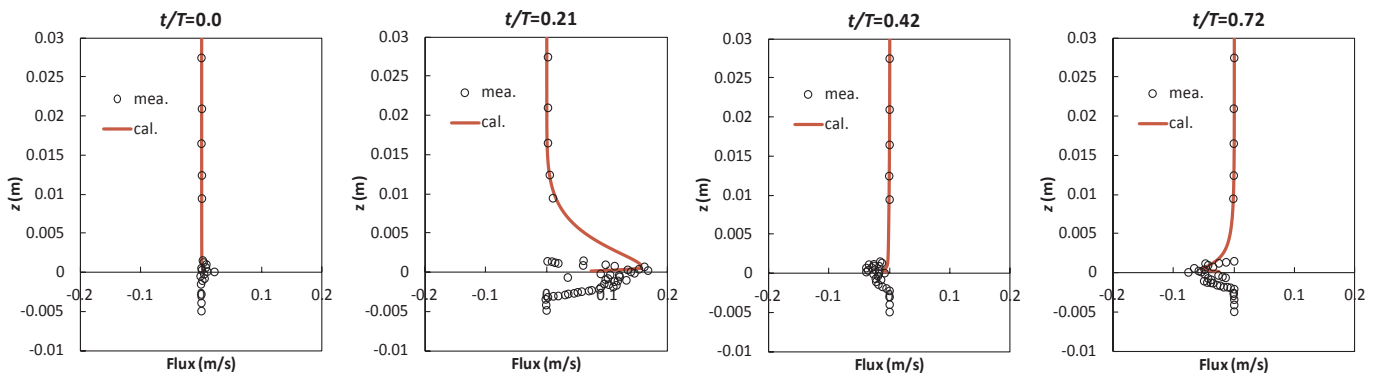
Fig. 17. Verification of flux profiles at selected phases for experiment MA5010 (values below 0 are in sheet flow layer which are not included in the model).
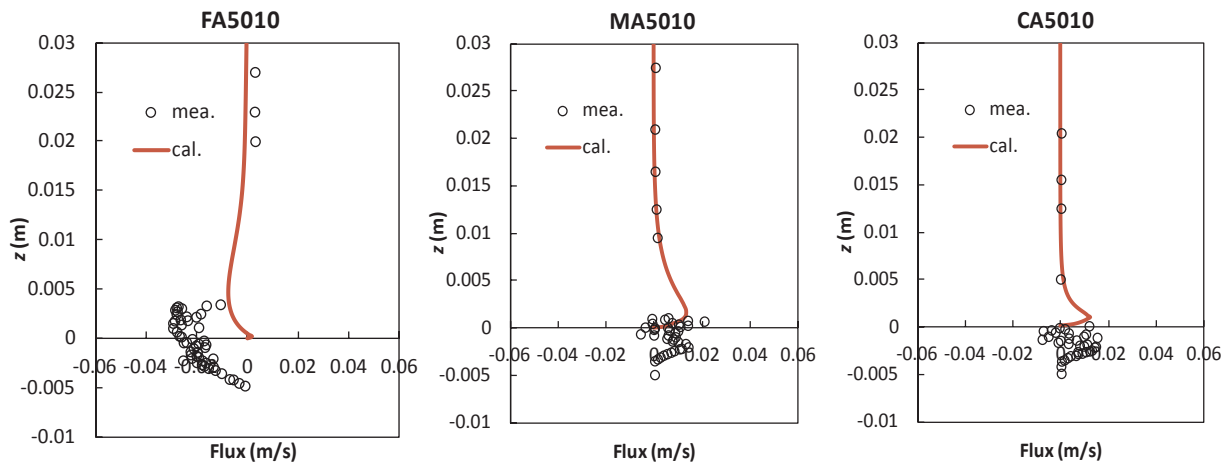
Fig. 18. Comparison of calculated and measured net flux profiles.
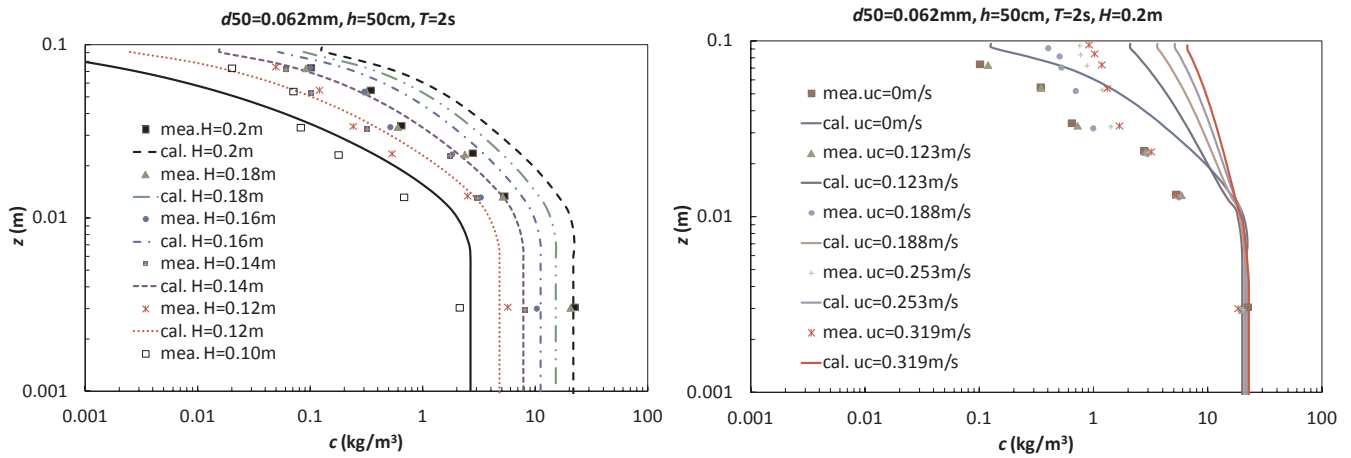
Fig. 19. Comparison of measured and calculated sediment concentration profiles (left: under wave-only conditions; right: under combined wave-current conditions).

$$x = -\frac{uh}{\alpha\omega_s}\ln(0.01) \tag{34}$$

Results show that, in Zhou and Ju (2007)'s case, the required distance of equilibrium concentration for $u_c = 0.123$–$0.319\,\text{m/s}$ (current-only) is about 82–212 m, and in the following Yao et al. (2015)'s case, the distance is about 65–276 m. According to Eq. (34), for sand particles with $d_{50} = 250$–$300\,\mu\text{m}$ under the conditions of $h = 0.3\,\text{m}$, $u_c = 0.3\,\text{m/}$ s, the required distance is about 9–12 m, which means that the 10–15 m is feasible for sand experiments. However, for silt sediment, the required distance for equilibrium is indeed longer, which is in line with the general knowledge. Under combined wave-current conditions, the equilibrium distance is far more complex than the steady current, which is not a simple theoretical derivation but need more sophisticated models (such as 2DV or 3D) to study this issue. Theoretically, the required equilibrium distance under combined wave-current conditions may be shorter than the steady flow because of the high oscillatory motion of waves. Besides, the stratification effects were not considered during derivation, which may also bring discrepancy. The above results are just for steady current and not so precise for combined wave-current conditions, but it provides a frame of reference which supports our interpretation of non-fully developed experiment conditions.

Under wave-only conditions, the calculated sediment concentration agreed well with the measured data. While under combined wave-current conditions, the calculated sediment concentration (equilibrium) was larger than the measured value (non-equilibrium), which might be caused by un-fully developed sediment concentration during the experiments. However, this is still an unresolved question and the non-equilibrium concentration can be further simulated by a 2DV model

considering longitudinal diffusive transport. Despite of the discrepancies between the computed and measured data, the model is able to simulate that the sediment profile became straighter as the current velocity increased. In the lower part, below about two times of the ripple height, the profiles change little which indicates that waves dominate the sediment suspension near the bottom; while in the upper part, the concentration increases with the increase of the current velocity, which indicates that the currents dominate the sediment suspension in the upper part.

3.2.4. Li (2014)'s flume wave case

Li (2014)'s experimental data was employed to verify the model under rippled bed. The sediment was silt and very fine sand with d_{50} of 0.045 mm and 0.11 mm. The experimental wave heights were 0.12 m, 0.15 m, 0.18 m, 0.21 m, and the water depth was 0.5 m. Fig. 20 shows the comparison of the measured and the calculated mean sediment profiles under different wave conditions as well as different sediment grain sizes. It can be seen that the sediment concentration near the bottom increased when the wave height increased. The sediment concentration profiles under waves were reasonably simulated by the model, with the RMSEs are 0.40–1.7 and 0.88–3.4 for the cases of $d_{50} = 0.045\,\text{mm}$ and 0.11 mm, respectively.

3.2.5. Yao et al. (2015)'s experiment

Yao et al. (2015) conducted a series of flume experiments to investigate sediment transport of sand-silt mixtures in both wave-only and wave-current conditions. Two types of sediments were used: a silt-sized mixture with a median grain size of 46 μm, and a very fine sand-
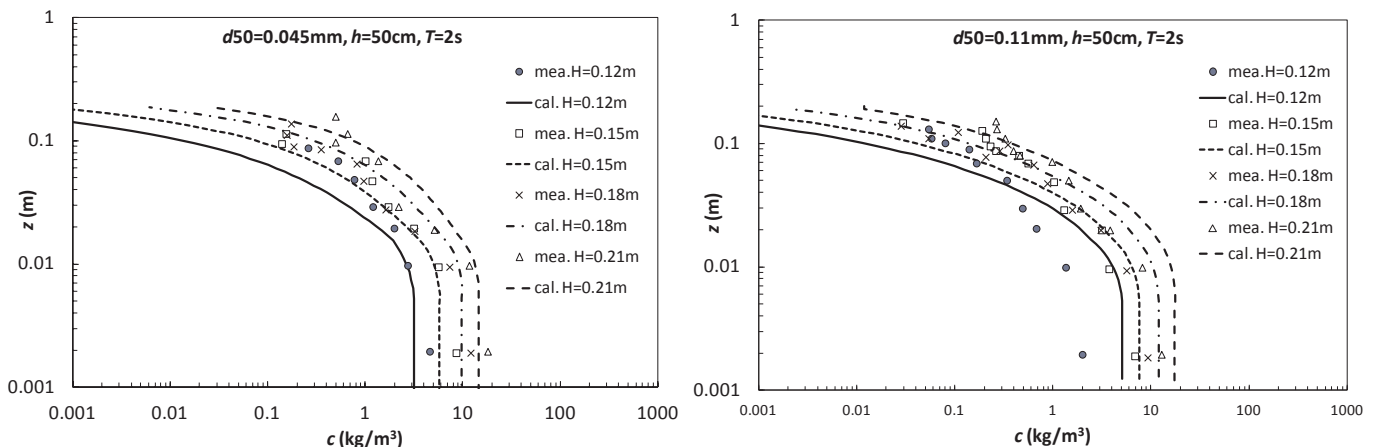
Fig. 20. Comparison of the measured and the calculated sediment concentration profiles (Li (2014)'s experiment) (left: $d_{50} = 0.045\,\text{mm}$; right: $d_{50} = 0.11\,\text{mm}$).

Table 5
Experimental conditions of Yao et al. (2015).

Case	h (m)	H (m)	T (s)	u_c (m/s)	Ripple height (cm)	Ripple length (cm)	Bed forms
s1-09	0.30	0.088	1.5	0	0.88	5.09	Rippled bed
s1-11	0.30	0.106	1.5	0	0.77	4.95	Rippled bed
s1-13	0.30	0.133	1.5	0	0.66	4.82	Rippled bed
s1-f3212	0.30	0.115	1.5	0.32	–	–	Flat bed
s1-o3812	0.30	0.12	1.5	−0.38	–	–	Flat bed
s2-09	0.30	0.091	1.5	0	0.83	5.48	Rippled bed
s2-10	0.30	0.10	1.5	0	0.75	4.73	Rippled bed
s2-12	0.30	0.12	1.5	0	0.8	6.13	Rippled bed
s2-f3311	0.30	0.106	1.5	0.33	1.58	8.45	Rippled bed
s2-o3911	0.30	0.11	1.5	−0.39	1.34	8.66	Rippled bed
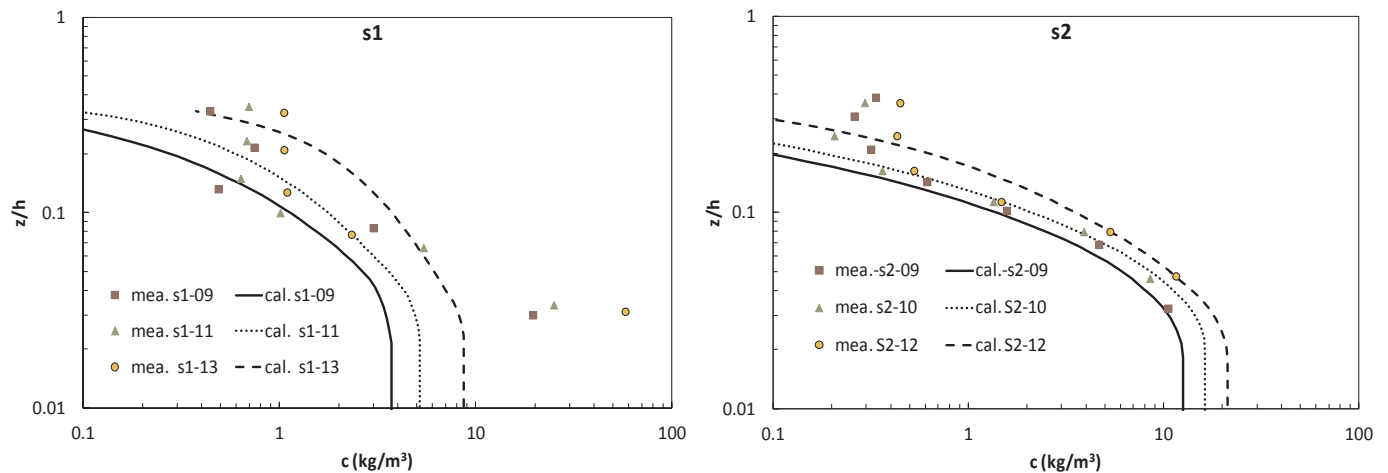
Fig. 21. Comparison of calculated and measured sediment concentration profile under wave-only cases of Yao et al. (2015)'s experiment.

sized mixture with a median grain size of 88 μm. The experiment conditions are listed in Table 5. Fig. 21 and Fig. 22 show the measured and calculated sediment concentration profiles under wave-only and wave-current conditions. It can be seen that the calculated sediment concentration fits well with the measured data near the bottom. The RMSEs are 0.87–1.58 and 0.49–0.82 for s1 (except the lowest measured data) and s2, respectively. There is larger discrepancy for s1 sediment, likely because larger mixture of sediments and two-layer bed morphology were detected during the experiments (Yao et al., 2015), i.e., silt-dominant and sand-dominant layers.

Under combined wave-current conditions, the sediment diffused to the upper part and the sediment concentration profile was much straighter, which was similar to Zhou and Ju (2007)'s experiment. The length of the sediment section in Yao et al. (2015)'s experiment was 15 m, which was longer than that in Zhou and Ju (2007)'s experiment. However, this length is still not long enough to avoid the occurrence of non-equilibrium sediment concentration under the wave-current condition; this was mentioned in Yao et al. (2015) too. Furthermore, for s1-f3212 and s1-o3812 case, when currents were imposed, ripples disappeared as presented by the author, and the sediment concentration
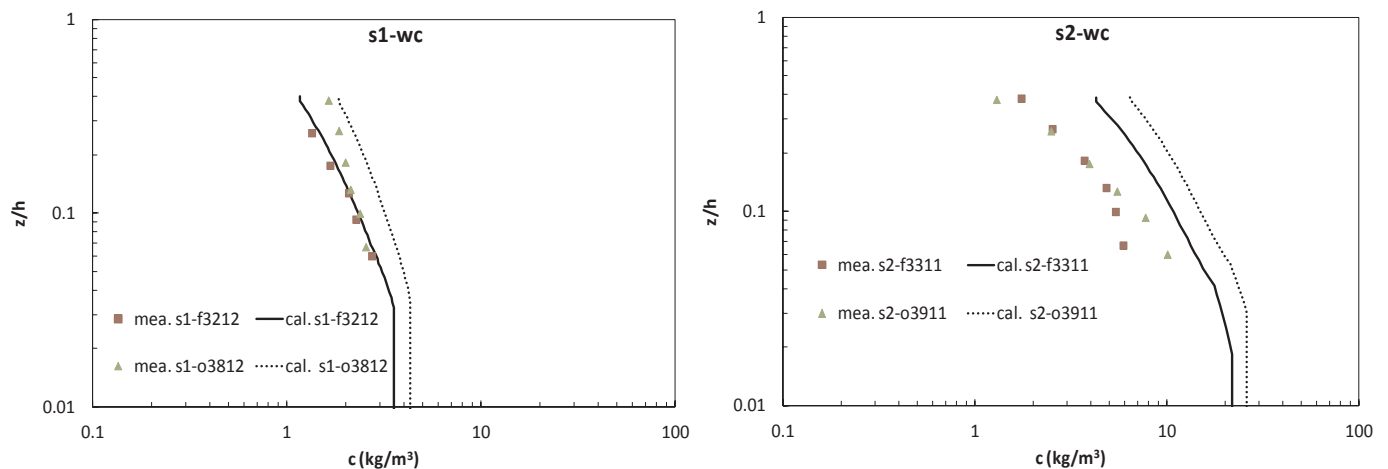
Fig. 22. Comparison of calculated and measured sediment concentration profile under wave-current cases of Yao et al. (2015)'s experiment (left: flat bed; right: rippled bed).

Table 6
Calculation conditions of sensitivity study.

Case	h (m)	u_m (m/s)	T (s)	u_c (m/s)	mobility number	d_{50} (mm)	bed types
d1-1	0.3	0.12	3	0	14.3	0.062	ripple
d1-2	0.3	0.20	3	0	39.8	0.062	ripple
d1-3	0.3	0.25	3	0	62.2	0.062	ripple
d1-4	0.3	0.30	3	0	89.7	0.062	ripple
d1-5	0.3	0.35	3	0	122.1	0.062	ripple
d1-6	0.3	0.38	3	0	143.9	0.062	ripple
d1-7	0.3	0.50	3	0	249.1	0.062	sheetflow
d1-8	0.3	0.55	3	0	301.4	0.062	sheetflow
d1-9	0.3	0.60	3	0	358.7	0.062	sheetflow
d1-10	0.3	0.65	3	0	421.0	0.062	sheetflow
d1-2uc05	0.3	0.20	3	0.05	42.3	0.062	ripple
d1-2uc10	0.3	0.20	3	0.10	49.8	0.062	ripple
d1-2uc15	0.3	0.20	3	0.15	62.3	0.062	ripple
d1-2uc20	0.3	0.20	3	0.20	80.0	0.062	ripple
d1-2uc25	0.3	0.20	3	0.25	102.1	0.062	ripple
d1-9uc05	0.3	0.60	3	0.05	361.2	0.062	sheetflow
d1-9uc10	0.3	0.60	3	0.10	368.7	0.062	sheetflow
d1-9uc15	0.3	0.60	3	0.15	381.1	0.062	sheetflow
d1-9uc20	0.3	0.60	3	0.20	398.6	0.062	sheetflow
d1-9uc30	0.3	0.60	3	0.30	448.4	0.062	sheetflow
d1-9uc40	0.3	0.60	3	0.40	518.2	0.062	sheetflow
d1-9uc50	0.3	0.60	3	0.50	607.8	0.062	sheetflow
d1-9uc60	0.3	0.60	3	0.60	717.4	0.062	sheetflow
d1-11uc60	0.30	1.00	3	0.60	996.4	0.062	sheetflow
d2-9	0.3	0.60	3	0	358.7	0.045	sheetflow

Note: the advection term is not included during simulation.

decreased without the vortexes' effects compared with that of s1-09 ~ s1-13. It indicates that the model is able to simulate sediment concentration distribution relating to bed forms. During simulation, the revised van Rijn (2007b)'s formula by Yao et al. (2015) (Eq. (26)) was employed for reference concentration. This formula is mainly for rippled bed. In this paper, however, the time-variant bed-shear stress with stratification effect was also used for silt simulation under 'flat bed' conditions and showed reasonable results.

4. Sensitivity analysis and discussion: factors that impact the sediment concentration profile of the HCL

Based on the validated experimental data, it is clear that a high concentration layer usually develops near the bottom under wave-dominant conditions. As sediment suspension occurs due to the turbulence diffusivity, the HCL is affected by the wave BBL. Under different bed forms, the eddy viscosity distribution as well as the sediment diffusion is different. Stratification effects may be an important impact factor on the HCL and the question is whether the stratification brings the collapse of turbulence. Sensitivity analysis was carried out using the 1DV model (the calculation conditions were listed in Table 6), focused on the factors which would influence the HCL:

- The relation of the HCL and the wave BBL;
- Effects of stratification;
- Effects of bed forms: vortex diffusion induced by ripples and eddy diffusion of flat bed (sheet flow);
- Effects of mobile bed roughness; and
- Effects of hindered settling.

Fig. 23 and Fig. 24 show the results of the 1DV model based on calculation conditions of d1-2 and d1-9, i.e., the intra-wave process of velocity profile, eddy viscosity profile and sediment concentration profile over rippled bed and plane bed.

4.1. The generation of the HCL

(1) The relation of the HCL and the wave BBL

The formation of the HCL is strongly related to the turbulence production inside the wave BBL. From Fig. 23(a) and Fig. 24(a) we can see that, the velocity gradient and the turbulence eddy viscosity are higher near the bottom, which mean higher shear stress and can cause sediment entrainment. However, in wave-dominated conditions, because of high oscillatory motion, the turbulence diffusion is depressed, which affects the SSC diffusion. In Fig. 23(a), we can see that the eddy viscosity decreases abruptly at about 0.03 m; while in Fig. 24(a), the eddy viscosity decreases abruptly at about 0.02 m. If a current is imposed, comparing Fig. 23(a) and (c) and Fig. 24(a) and (c), the turbulence diffusion will be more uniform and the c profiles will become uniform too. It means that the interface of HCL will be affected by current. The relation of HCL and BBL will be discussed by the calculation results in the following, and the role of current will be discussed in next part.

For silt with a diameter of 62 μm, calculations were carried out with increasing orbital velocity and mobility number under oscillatory wave motions. Fig. 25 shows the mean sediment concentration profiles and maximum orbital velocity profiles near the bed. With the increasing of the mobility number, the bed forms of the study cases change from rippled bed to flat-bed (sheet flow). Fig. 26 shows the eddy viscosity distribution under different wave conditions, and Fig. 27 shows the ripple parameters. In this study, the height of the HCL is defined where the gradient of the sediment concentration changes abruptly. For ripple cases d1-1 to d1-6, the HCL height varies at about 1.3–2.2 cm, and the corresponding wave boundary layer thickness is about 0.6–1.1 cm. For sheet flow cases d1-7 to d1-10, the HCL height varies at about 1.2–1.5 cm, and the corresponding wave boundary layer thickness is about 0.55–0.70 cm. The thickness of the HCL is about twice the wave boundary layer, as referred in some literature (e.g., Yao et al., 2015). It
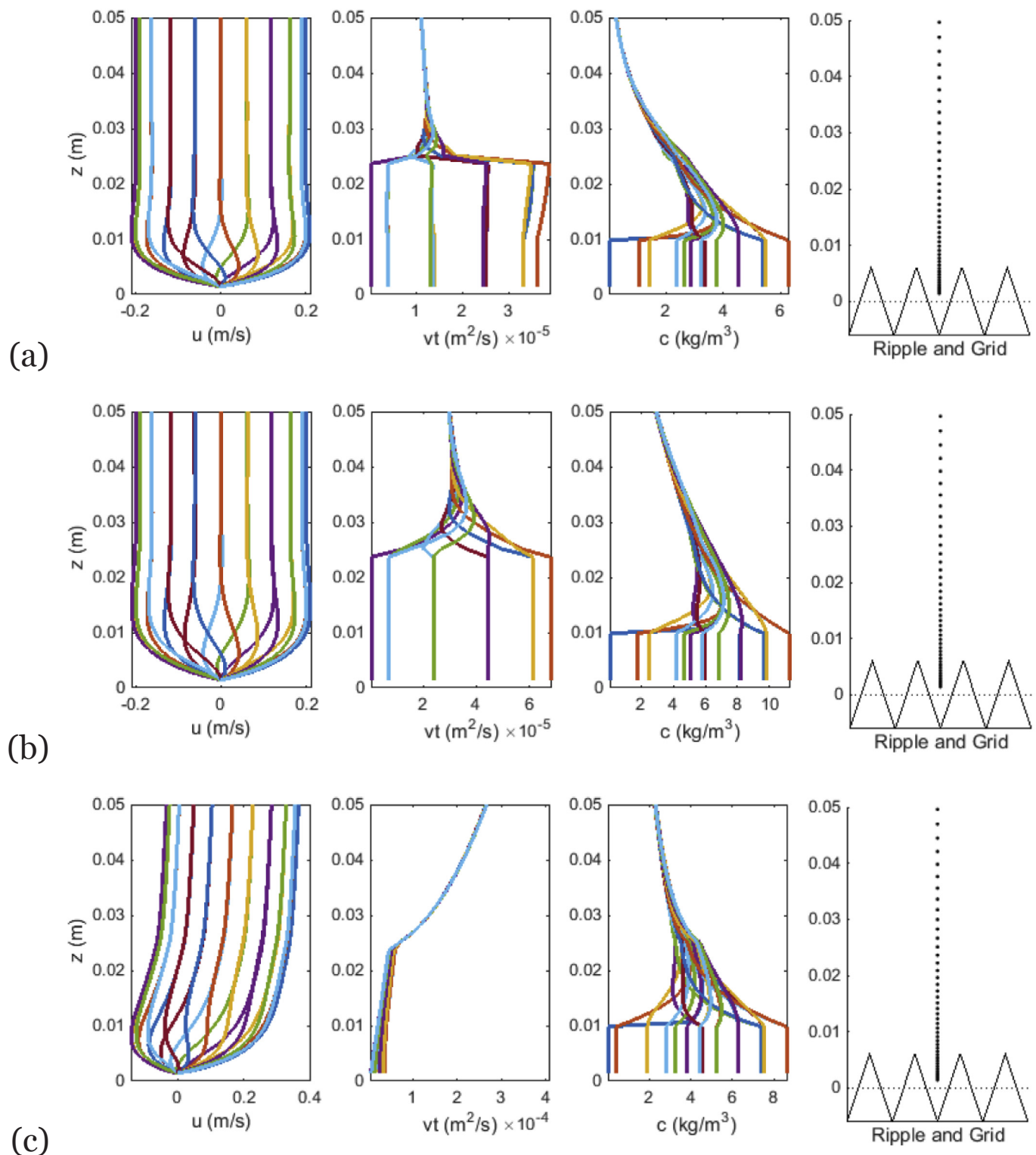
Fig. 23. Intra-wave process of velocity profiles (left column), eddy viscosity profiles (middle column) and sediment concentration profiles (right column) over rippled bed calculated by the 1DV model (The calculation conditions were based on d1-2. (a): wave only case with stratification effects; (b): wave only case without stratification effects; (c): wave-current case with $u_c = 0.20\,\text{m/s}$.

means that, although the velocity is restricted in the BBL, the eddy viscosity as well as the diffusion viscosity can still reach higher levels.

For the rippled bed cases, as the flow dynamics increase, the ripple height and ripple length increase first and cause the HCL to become thicker, then they decrease after reaching a maximum (case d1-3), see Fig. 27. However, for case d1-3 to d1-6, although the ripple height

decreases, the wave boundary thickness increases with stronger flow dynamics, and the reference concentration becomes larger, which induces a thicker HCL; however, suspended sediment concentration above the HCL is lower from case d1-3 to d1-6, which is caused by the lower ripple height. Compared case d1-6 (rippled bed) with case d1-7 (sheet flow), although the flow dynamic is stronger in case d1-7, the
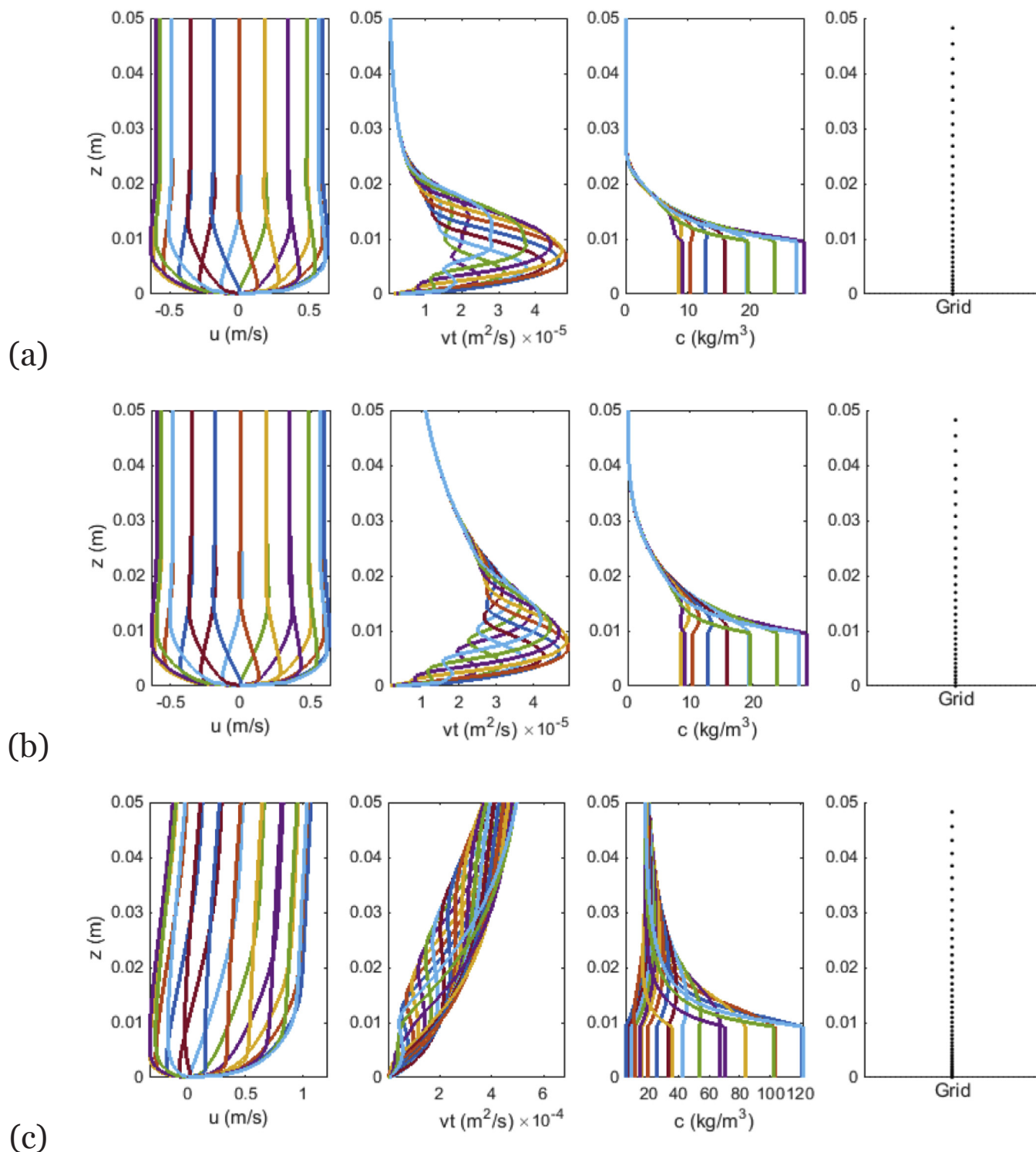
Fig. 24. Intra-wave process of velocity profiles (left column), eddy viscosity profiles (middle column) and sediment concentration profiles (right column) in sheet flow conditions calculated by the 1DV model (The calculation conditions were based on d1-9. a: wave only case with stratification effects; b: wave only case without stratification effects; c: wave-current case with $u_c = 0.60\,\mathrm{m/s}$.

sediment concentration is lower, and the suspension height is lower than that for d1-6 because of the lower eddy viscosity (Fig. 26) and thinner wave boundary layer (Fig. 25). From d1-7 to d1-10, with stronger flow dynamics, the sediment concentration increases again, and the HCL develops when the BBL becomes larger too. Thus, it is concluded that we could directly establish the relation between the HCL and the BBL, as the BBL is affected by both bed forms and flow

dynamics. It is not appropriate to relate the HCL with a single factor, e.g., simple ripple parameters or flow parameters.

(2) The role of wave and current on the HCL

When a current is imposed, i.e., under combined wave-current conditions, the sediment concentration profile changes significantly,
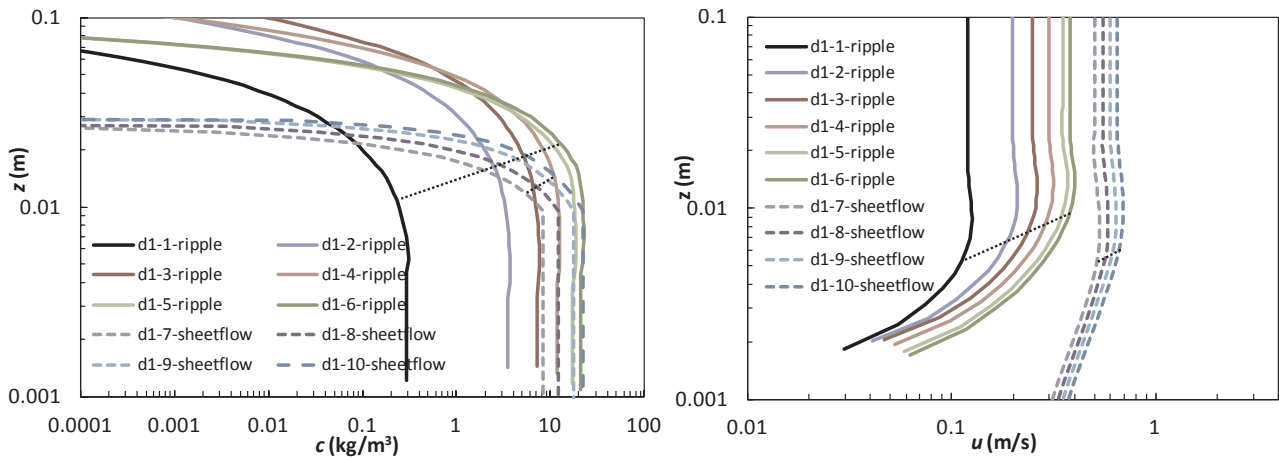
Fig. 25. Sediment concentration profiles (left) and maximum orbital velocity profiles (right) near the bed.
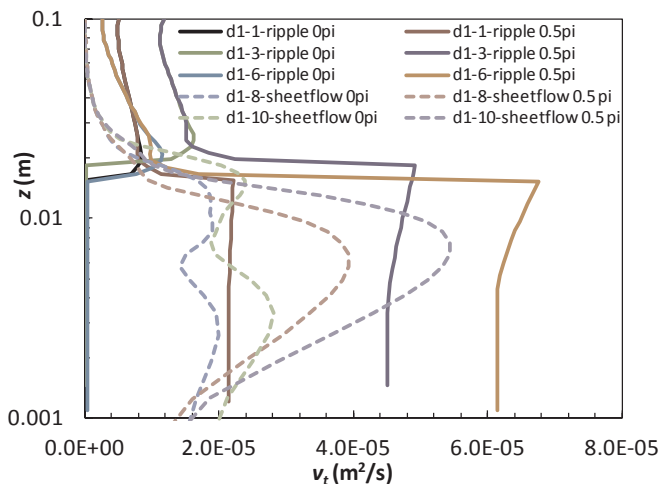
Fig. 26. Eddy viscosity distribution under different wave conditions.
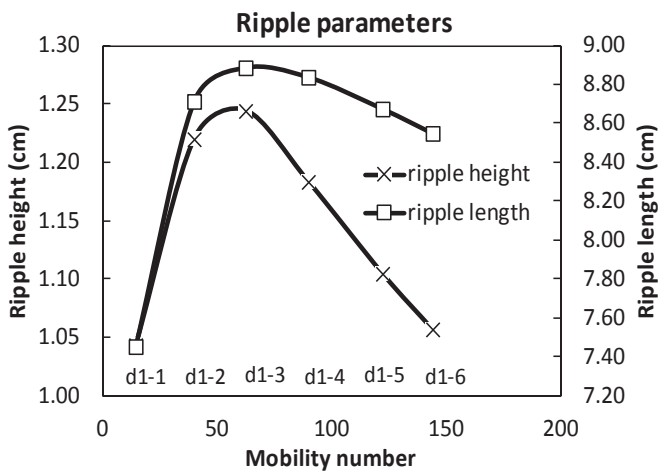
Fig. 27. Ripple parameters under different wave conditions.

with much higher suspension and even an uniform value across the entire water depth, which has been proven by many experiments, for example Zhou and Ju (2007) and Yao et al. (2015). Fig. 28 shows the vertical distribution of the sediment concentration, eddy viscosity and maximum velocity under different combined wave-current conditions. The ratio of the current velocity to the wave max orbital velocity varies from 0 to 1. It can be seen that the sediment concentration near the bottom is dominated by waves and beyond the wave boundary layer the

sediment concentration is greatly influenced by currents. The eddy viscosity plays a dominating role in sediment suspension. With different currents, the eddy viscosity changes little in the wave boundary layer, but changes significantly in the upper part, which corresponds to the changes of sediment concentration profile. It needs to be stated that the mobile bed effects were considered in the calculation, which may change the wave boundary layer under different wave-current conditions.

Over rippled beds, the changes of sediment concentration distribution has similar tendency under different wave-current conditions. The evidence of experimental data has been shown by Zhou and Ju (2007) and Yao et al. (2015), and the data of Yao et al. (2015) is shown in Fig. 29. To avoid the influence of ripples, sensitivity calculations were carried out by fixing the ripple parameters and changing only the current velocity. The results are shown in Fig. 30. It can be seen that the changes of the sediment concentration profile are similar to those under sheet flow conditions. The vortex layer did not change as the ripples were fixed, thus the sediment concentration near the bottom did not change. Beyond the vortex layer, the sediment concentration increases significantly when currents are imposed.

(3) The role of the stratification effects

The stratification effects contribute to the formation of the HCL as the sediment diffusivity is further decreased from turbulence damping. Stratification effects have been proved to have impacts on flow dynamics and sediment concentration profiles of mud (Winterwerp, 2001), and the results showed that stratification effects cause collapse of turbulence and greatly reduce the mud sediment concentration. From the experimental data of Dohmen Janssen et al. (2001) and Zhou and Ju (2007), as well as assumed simulation cases, we did a preliminary study on the stratification effects. The sediment grain size varied from medium sand $d_{50} = 0.21$ mm, fine sand $d_{50} = 0.13$ mm to silt $d_{50} = 0.062$ mm. Figs. 31–33 show the comparison of the sediment concentration with and without stratification effects. It can be seen that stratification effects decrease the turbulence and concentration profile, which is in line with the general understanding. Sediment stratification is a non-negligible factor for silt and very fine sand.

Fig. 33 shows the comparison of the sediment concentration and eddy viscosity with and without stratification effects for silt of $d_{50} = 0.062$ mm and 0.045 mm. The results show that the eddy viscosity decreases greatly above the wave boundary layer, but changes little near the bottom. Above the HCL, the stratification decreases the eddy viscosity (or sediment diffusivity) greatly, and shows a collapsing behavior, which is similar to fluid mud (Winterwerp, 2001). The damping of turbulence contributes to the formation of the HCL, as the decreased diffusivity cannot sustain the sediment suspension. As a
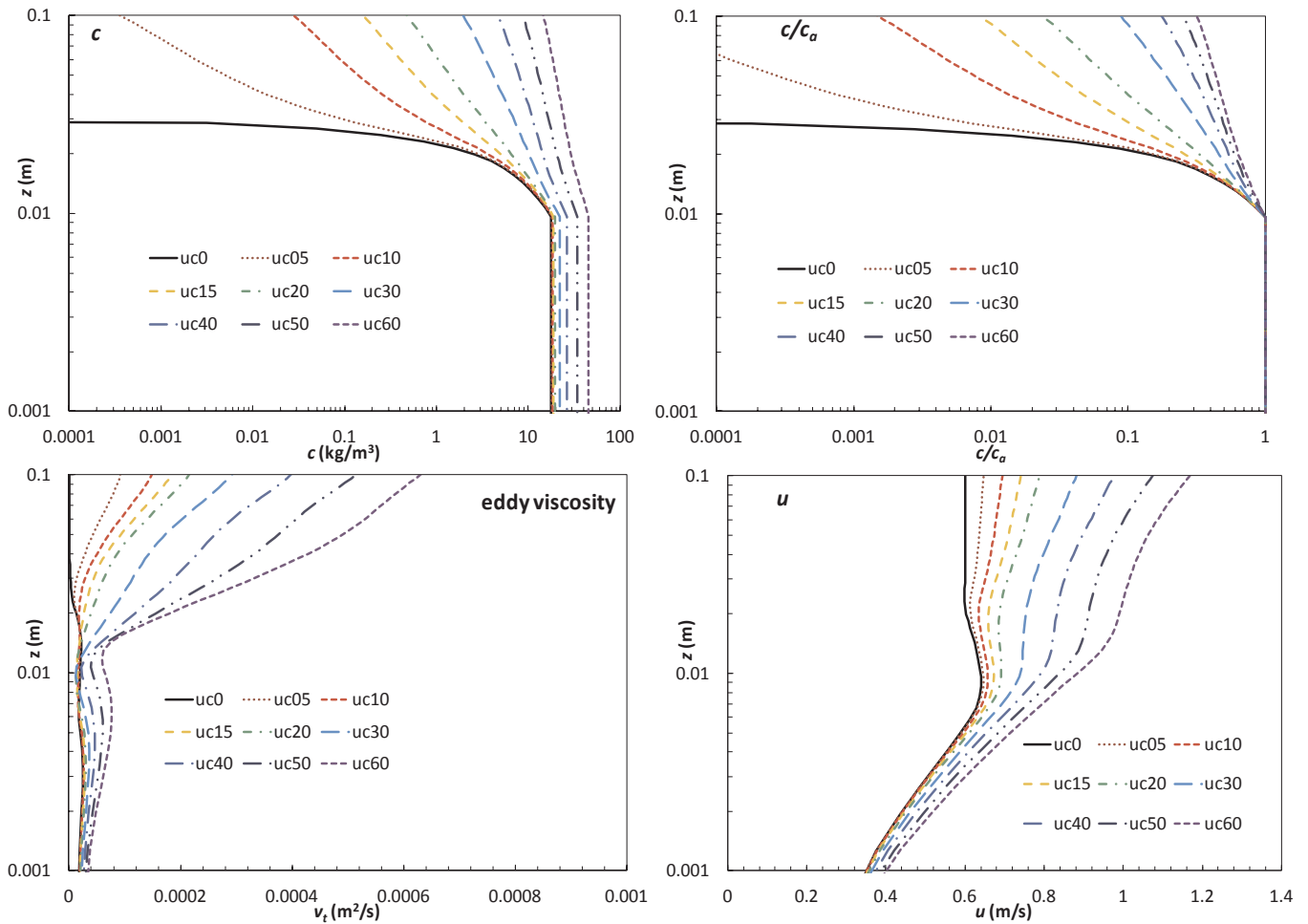
Fig. 28. Distribution of sediment concentration, the ratio of c/c_a, eddy viscosity and maximum velocity (u) under different wave-current conditions under sheet flow conditions (for waves: $u_{wmax} = 0.6$ m/s, $T = 3$ s, for currents: the depth-averaged velocity is represented by $uc0 = 0.0$ m/s, $uc05 = 0.05$ m/s, $uc10 = 0.10$ m/s, $uc15 = 0.15$ m/s, $uc20 = 0.20$ m/s, $uc30 = 0.30$ m/s, $uc40 = 0.40$ m/s, $uc50 = 0.50$ m/s, and $uc60 = 0.60$ m/s).
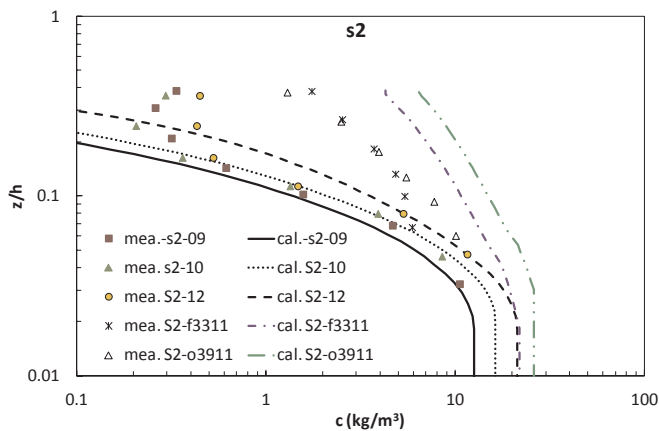
Fig. 29. Experimental data of sediment concentration profiles under wave and wave & current conditions (Yao et al., 2015) (wave only cases: s2-09, s2-10, s2-12; wave-current cases: s2-f3311, s2-o3911).

result, the concentration gradient becomes larger, which further increases the stratification effects. After equilibrium, a clear interface forms between the HCL and the upper clear water layer. However, near the bottom, the damping effects show little change, which shows the maintenance of the turbulence production. This is mainly because there is no flocculation process and the bottom consists of a consolidated layer, which is similar to sand but different from fluid mud. The

comparison of $d_{50} = 0.062$ mm and 0.045 mm shows that finer sediment causes larger damping effects. Thus, the stratification behavior of silt has the transitional behavior between sand and cohesive mud, i.e., unlike sand, the stratification effects cannot be neglected; however, unlike fluid mud, the stratification effects for silt is not strong enough to destroy the flow dynamics.

The flux Richardson number Ri_f or bulk Richardson number Ri_c is often used to describe the stratification effects. Winterwerp (2001) argued that a turbulent shear flow collapses when the flux Richardson number exceeds a critical value which was found to be a constant (0.15) under steady state. In Yao et al. (2015)'s experiment, it was concluded that the critical value of the bulk Richardson number can be affected by the grain size and it is difficult to relate the Richardson number with silt-enriched concentration. Conley et al. (2008) showed that the stratification effect is related to u_m/w_s independent of grain sizes, which provided a further direction to find a relation of stratification effect with the flow-dynamics.

4.2. Effects of bed forms on the SSC profiles

According to van Rijn (2007a), dune type bed forms are generally absent when the sediment bed is finer than about 100 μm, and the bed generally consists of a flat mobile surface or small-scale ripples. Baas et al. (2016) showed that ripples do exist for fine sediment or mixture sediment, not only for non-cohesive sediment but also for cohesive sediment. The dominant bed forms in oscillatory waves with or without a weak current in field conditions are often ripples with a length scale
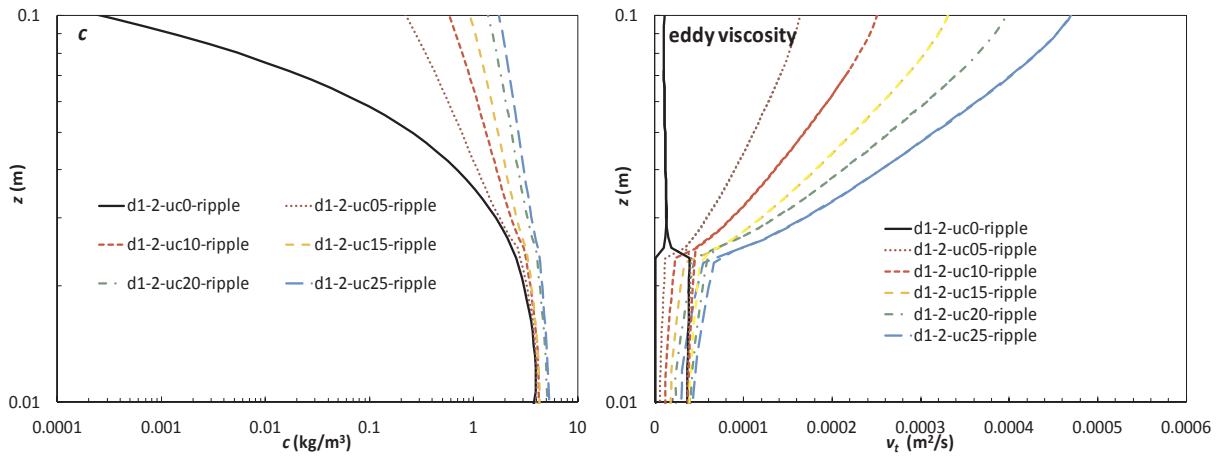
Fig. 30. Distribution of sediment concentration and eddy viscosity under different wave-current conditions over rippled bed (the ripple heights were fixed as the same).

related (smaller or equal) to the near-bed orbital diameter. The impacts of bed forms on sediment transport have been studied by some scholars, (e.g., Davies and Villaret, 2003; Styles and Glenn, 2003; Grasmeijer and Kleinhans, 2004; Myrhaug and Holmedal, 2007; Baas et al., 2016). In this paper we focus on the differences in simulation method and concentration profile shapes.

(1) Can we simulate the sediment concentration profile on rippled bed using the ´flat bed' method by adding the ripple-induced roughness?

To test the vortex's influence on the sediment concentration profile, Fig. 34 shows the comparison of the sediment concentration profile calculated using the rippled bed method and the 'flat bed' method, as well as the experimental data for comparison. The flow dynamics conditions are the same in the simulation. When using the 'flat-bed' method, the ripple-induced roughness (varies from 22 mm to 29 mm in this case) was considered which was much higher than the grain roughness (only 0.155 mm). It can be seen that the flat bed method results in much less concentration and fails to simulate the sediment concentration profiles. Under the same flow dynamics, the suspension on rippled beds by shedding of vortices is far greater than that of flat beds where no such coherent mechanism is present. The sediment concentration difference is several orders of magnitude between the two bed form conditions, especially in the upper part. This means that different approaches have to be employed to simulate the sediment concentration under different bed forms. The method which simply
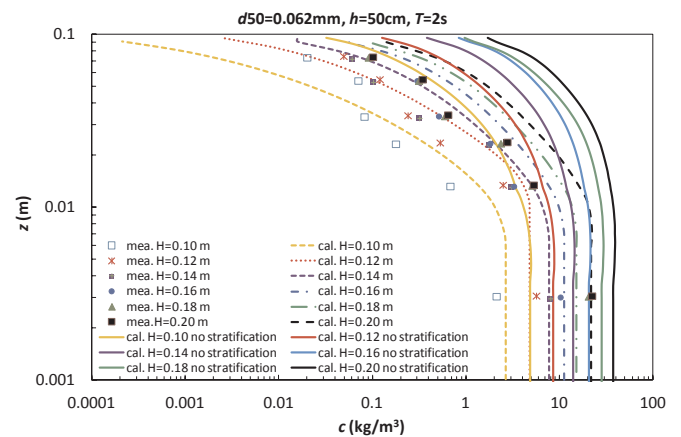
Fig. 32. Comparison of sediment concentration with and without stratification for silt with $d_{50} = 0.062$ mm (The measured data is from Zhou and Ju (2007)'s experiment under rippled-bed).

generalizes the ripples based on roughness cannot correctly simulate the sediment dynamics.

The experimental data of Yao et al. (2015) also showed this phenomenon. During the experiment of sediment s1 ($d_{50} = 44\,\mu m$), there were ripples in wave-only cases, and the ripples disappeared when currents were imposed (case s1-f3212 and s1-o3812). In this case,
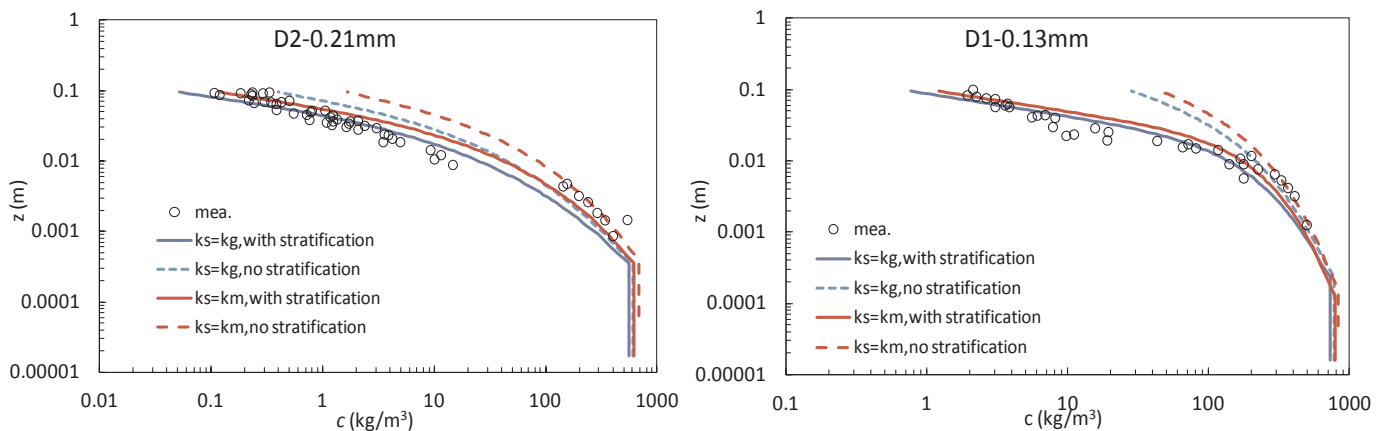
Fig. 31. Comparison of sediment concentration and velocity distribution: with or without stratification and with or without moving bed roughness (kg = grain roughness and km = mobile bed roughness. The experimental data is from Dohmen Janssen et al. (2001)).
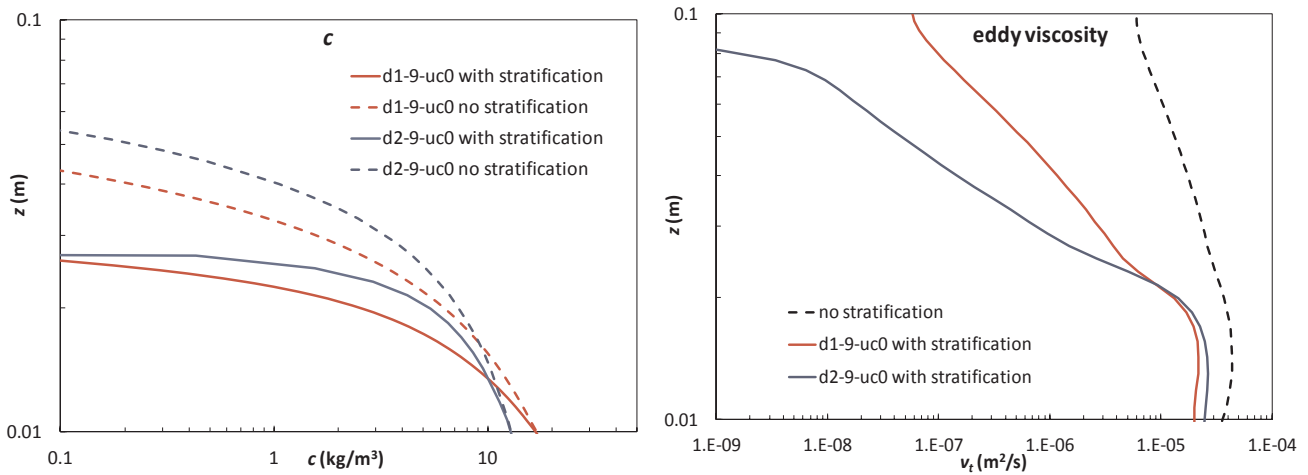
Fig. 33. Comparison of sediment concentration and eddy diffusivity with and without stratification effects ($d_{50} = 0.062$ mm (d1-9), $d_{50} = 0.045$ mm (d2-9), $T = 3$ s, and $u_m = 0.6$ m/s).

during the transition of rippled bed to flat bed, although the flow dynamics was stronger, the sediment concentration near the bottom decreased as the vortices disappeared (Fig. 35). Since rippled beds occur in relatively low wave conditions, this can lead to the paradoxical outcome that, for a given mean current strength, more sediment may be transported in the presence of small waves above rippled beds than by sheet flow beneath large waves above plane beds (Davies and Villaret, 2002; Davies and Thorne, 2005).

(2) The shape of sediment concentration profile under different bed forms

Are the shapes of the sediment concentration profiles similar under rippled bed and sheet flow conditions? To answer this question, Fig. 36 shows the sediment concentration profiles under different bed forms. It can be concluded that the profile shapes are different with different bed forms. The shape of HCL is determined by bed forms, while the value is determined by flow dynamics. It is not difficult to explain this phenomenon mainly because of the eddy viscosity distribution (Figs. 23 and 24) which was discussed earlier.
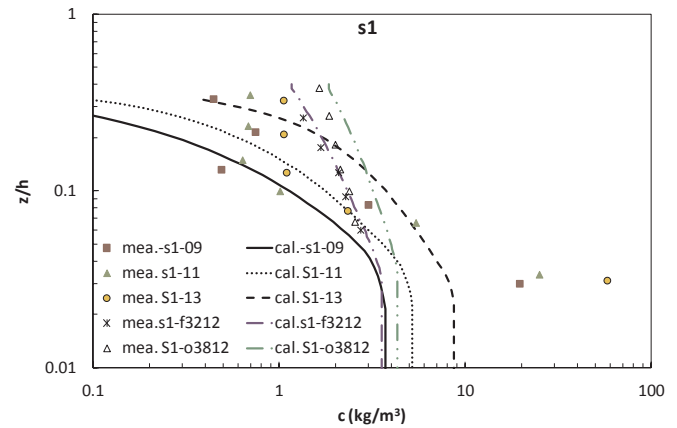
Fig. 35. Sediment concentration profiles under different conditions by Yao et al. (2015) (s1-09, s1-11, s1-12 were rippled bed cases and currents were imposed in case of s1-f3212 and s1-o3812).
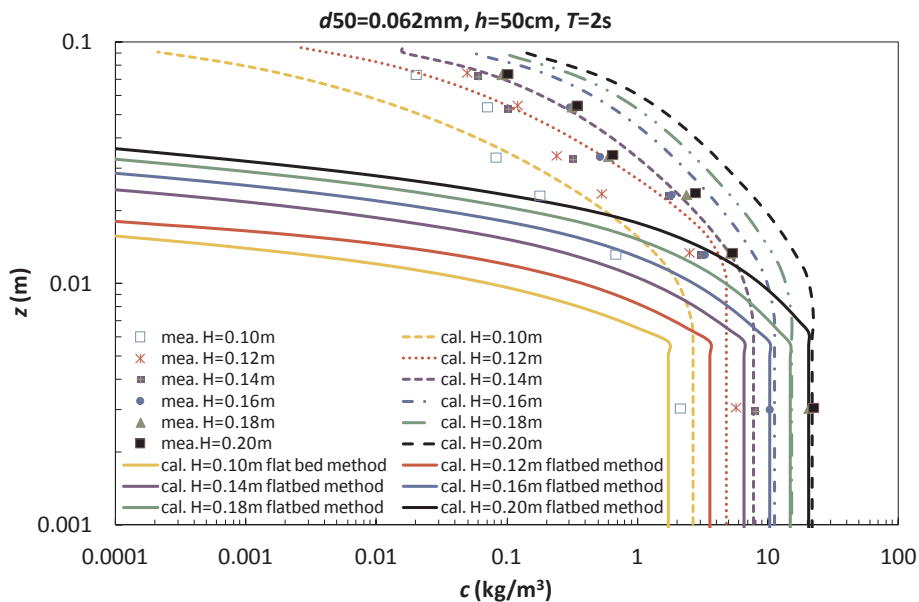
Fig. 34. Comparison of measured and calculated sediment concentration profiles under wave-only conditions (the measured date was Zhou and Ju (2007)'s case; the dot-lines were calculated using the 'rippled-bed' method, and the solid lines were calculated using the 'flat-bed' method).
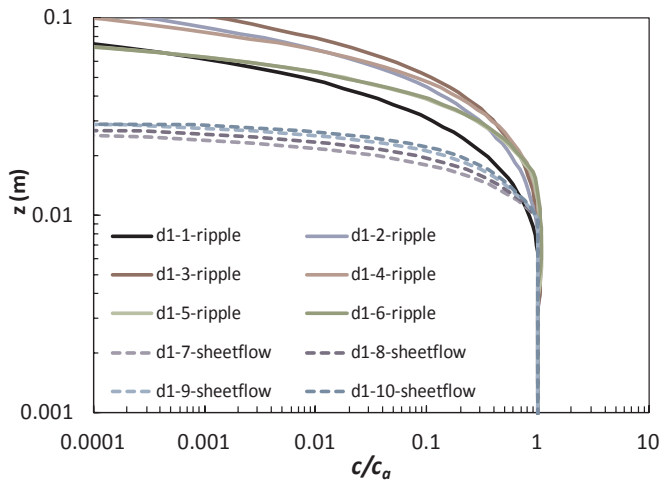
Fig. 36. Sediment concentration profiles on different bed forms (Lines represent rippled bed, and dash lines represent sheet flow).
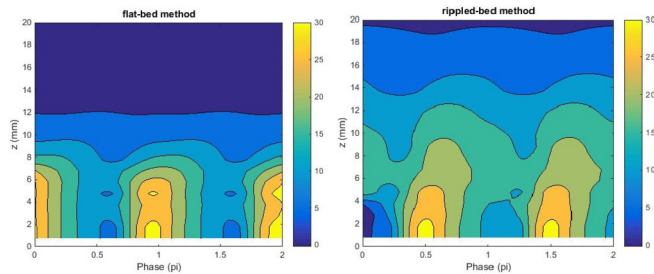
Fig. 37. Sediment concentration process within a wave period on different bed forms (unit: kg/m^3, left: using flat-bed method, right: using rippled-bed method, $H = 0.2$ m, $T = 2$ s, and $d_{50} = 0.062$ mm).
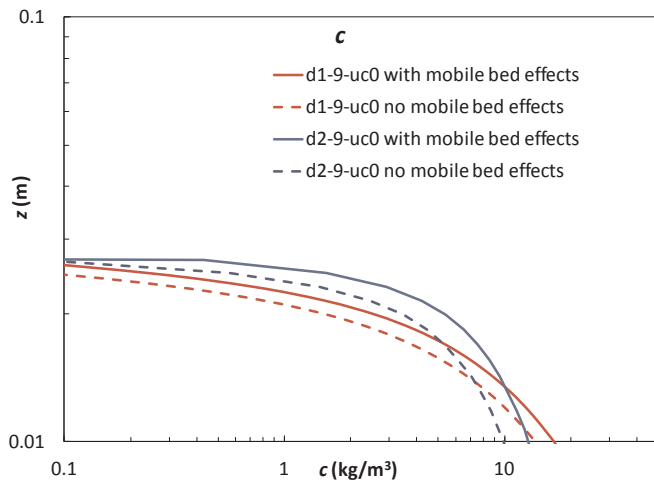
Fig. 38. Comparison of sediment concentration with and without mobile bed effects ($d_{50} = 0.062$ mm (d1-9), $d_{50} = 0.045$ mm (d2-9), $T = 3$ s, and $u_m = 0.6$ m/s).

Fig. 37 shows the time-series of sediment concentration contour under different bed forms. It can be seen that, under sheet flow conditions, the maximum concentration at the bottom happens nearly at the phase of maximum flow shear dynamics. While under rippled bed, it happens at the time of flow reversal because of the effects of the vortex. Besides, the figures also show the phase defection of sediment concentration in the upper part.

Bed forms are as important as flow dynamics for sediment transport, which means that we should not only analyze sediment transport with

flow dynamics but also should consider bed forms. In short, bed forms determine the shape of concentration profile near the bottom, and flow dynamics determines the value of sediment concentration under a bed type.

4.3. The effects of mobile bed on SSC profiles in HCL

From Dohmen Janssen et al. (2001)'s case and the assumed cases, we also tested the mobile bed effects on the sediment concentration profile under sheet flow conditions (see Figs. 31 and 38). It can be seen that the mobile bed affects the sediment concentration profile, i.e., taking the mobile bed roughness into consideration, the sediment concentration increases. In Fig. 31, the grain roughness and mobile bed roughness are 0.32 mm and 1.48 mm, respectively, for D1-0.13 mm. The grain roughness and mobile bed roughness are 0.53 mm and 1.88 mm, respectively, for D2-0.21 mm. The ratio of mobile bed roughness to grain roughness is 4.6 for D1-0.13 mm and 3.5 for D2-0.21 mm. For finer sediment, for example, silt with $d_{50} = 0.062$ mm and $d_{50} = 0.045$ mm in Fig. 38, the grain roughness is only 0.155 mm and 0.113 mm, respectively, which is too small and unrealistic. Therefore, the mobile bed roughness must be used in these cases, with the value of 0.58 mm and 0.47 mm, respectively. Here a 2.5 times of grain roughness was used as the simulation case of without mobile bed effects in Fig. 38. Results show that the sediment concentration near the bottom without mobile bed effects was 21–29% smaller than that with mobile bed effects. Thus, for fine sediment, the mobile bed roughness is dominant.

The intensive sheet flow layer leads to turbulence damping and increased flow resistance. The damping of turbulence decreases the sediment concentration while the mobile bed effects increase the sediment concentration. For medium sand, the stratification and mobile bed effects can be neglected, and some models received good results without considering the stratification and mobile bed roughness (e.g., Holmedal et al., 2004; Zhang et al., 2011a). However, for silt and fine sand, these physical processes are important impact factors, which cannot be neglected.

4.4. The effects of hindered settling on SSC profiles

Hindered settling of silt has been studied extensively by Te Slaa et al. (2015) and the results were given clearly on the influence of the SSC profile. Here we do not study the mechanism of hindered settling velocity, but only give the sensitivity comparison with and without hindered settling, see Fig. 39, taking the silt of $d_{50} = 0.062$ mm as an example. It can be seen that, the effects of hindered settling velocity
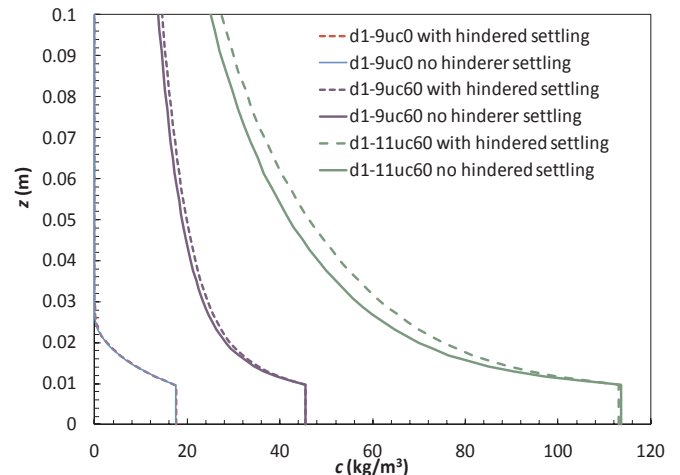
Fig. 39. Comparison of sediment concentration with and without hindered settling velocity.
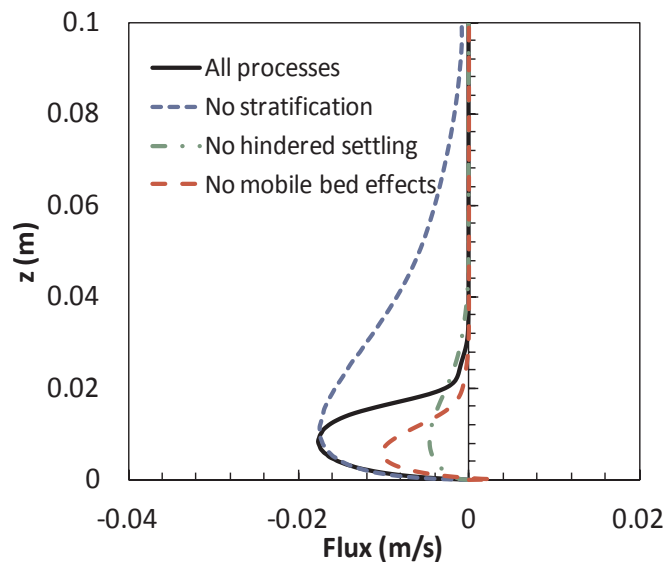
Fig. 40. The wave-induced net flux considering different physical processes (based on the experiment conditions of O'Donoghue and Wright (2004); "All processes" means the effects of stratification, hindered settling and mobile bed effects are considered).

impact the SSC profiles when SSC is high, for which the SSC becomes higher due to lower settling velocity. For case d1-9uc0 ($u_m = 0.6$ m/s) with the reference concentration of 17.6 kg/m^3, the hindered settling velocity almost has no effects on the SSC profile; for case d1-9uc60 ($u_m = 0.6$ m/s and $u_c = 0.6$ m/s) with the reference concentration of 45.6 kg/m^3, the SSC is higher by about 5% with the effects of hindered settling velocity; and for case d1-11uc60 ($u_m = 1.0$ m/s and $u_c = 0.6$ m/ s) with the reference concentration of 113 kg/m^3, the SSC is higher by about 10% with the effects of hindered settling velocity. For high SSC simulation, the hindered settling velocity is a non-ignorable impact factor.

4.5. Preliminary sensitivity analysis on wave-induced net sediment flux

Sediment flux is a combined result of flow-sediment dynamics. Lacking of the measured data of sediment flux in the experiments for silty sediments (such as Yao et al., 2015, Zhou and Ju, 2007 and Li, 2014), the model is still not well verified on the net sediment flux. Thus, this paper does not address much about the sediment flux. However, the sediment flux data of O'Donoghue and Wright (2004) for fine sand was collected to verify the model. Based on the wave conditions of case FA0510 in O'Donoghue and Wright (2004), we preliminary analyzed some impact factors on the net sediment flux, including the effects of stratification, hindered settling and mobile bed. The medium grain size was reduced to be 0.11 mm.

Fig. 40 shows the wave-induced net flux profiles considering different physical processes. It can be seen that, the stratification effects reduces the flux, which is in line with the changes of sediment concentration analyzed above. If integrated from the bottom to 0.1 m, the integrated flux decreased about 62% compared that without stratification effect. Hindered settling will increase the net flux because of the lower settling velocity, which also means sediment flux will decrease if the hindered settling is not considered; according to this case, the integrated flux decreased by 64% compared with that considering hindered settling. Similarly, the sediment flux will decrease without mobile bed effects, with the decrease ratio of the integrated net flux of 56% in the study case. Results show that, the effects of stratification, hindered settling and mobile effects are important and non-negligible factors for fine sediment transport. The flux of silty sediment still needs further study, and more measured data are expected.

4.6. Discussion

For silt and fine sand, in wave-dominated environment, there is a high sediment concentration layer (HCL) near the bed bottom, which is about twice the height of the wave boundary layer. From above sensitivity analysis, we can see that, one of the main reasons of the formation of the HCL is that the eddy viscosity is limited within the BBL and it is difficult for the sediments to suspend to the upper part. When currents are imposed, the SSC profile becomes smoother and the upper part becomes turbid. The stratification effects contribute to the formation as the sediment diffusivity is further decreased from turbulence damping. Another reason lies in the hindered settling effects which induces lower effective settling velocity of the sediment lower in the water column than that in the upper part, similar to the so-called lutocline (Winterwerp, 1999).

Silt shows transition behavior between sand and cohesive clay. Winterwerp (2001) has elaborately described the behavior of non-cohesive and cohesive sediment. Suspensions of non-cohesive sediment under steady state conditions are characterized by equilibrium concentrations. The turbulence damping effect is not strong on deposited sand rigid bed, and turbulence production remains possible. Although there is still likely a very thin HCL on the sand bed, due to the relatively high settling velocity, the HCL cannot fully develop and bed load sediment transport is the main movement type. For cohesive sediment, because of flocculation processes, the deposited sediments do not form a rigid bed but cause a layer of fluid mud to form, thus create a two-layer fluid system. At the interface between the two-layer fluid, vertical turbulent mixing is strongly damped and results in a catastrophic collapse of the vertical turbulence field and the vertical sediment concentration profile. Even under steady current or combined wave-current conditions, a distinct interface of fluid mud can still be investigated. Due to the strong damping effects, the HCL of silt may share a similar two-layer system as fluid mud. However, from above sensitivity analysis we can see that because of little flocculation of silt, although there is a turbulence collapse above the HCL, the turbulence in the wave boundary layer near the bottom can still be maintained. The equilibrium concentration concept may still be applicable for silt, but the stratification effects have to be included. Another important difference to fluid mud is that the HCL of silt only exists in wave dominant conditions, because when a current is imposed, diffusion becomes large in the upper part and the interface is destroyed.

5. Conclusion

A 1DV model was established for flow-sediment dynamics in the wave-current bottom boundary layer, especially for simulation of the HCL of silt and very fine sand. Based on the physical background, special approaches for sediment movement were introduced, including approaches for different bed forms (rippled bed and 'flat-bed'), hindered settling, stratification effects, mobile bed effects, reference concentration and critical shear stress. For rippled beds, the combined vortex and k-ε model was employed to simulate the turbulence and the k and ε values at the interface of the vortex-dominated layer were derived. For sheet flow conditions, mobile bed effects were considered which are important for fine grain size sediment transport. The approaches of hindered settling were employed considering the difference between silt and sand. An expression of silt-sand incipience of motion was employed for the critical shear stress. During the reference concentration calculation, it is unrealistic to give a zero value for the bed concentration during the stage of a wave cycle, when the shear stress is lower than the critical value. To overcome this shortcoming, the reference concentration was revised by considering the deposited sediment from the last time step. A number of experimental datasets were used to verify the model, which showed that the model is able to simulate the flow dynamics and sediment concentration profiles reasonably, for sheet flow conditions and rippled bed, as well as silt and sand.

A HCL near the bottom is one of the most important characteristics of silty sediments. Sensitivity analysis was carried out on the factors impacting the HCL, i.e., bed forms, flow dynamics, and effects of stratification, mobile bed and hindered settling. The results showed that 1) The formation of the HCL is related to the turbulence production inside the wave BBL: the eddy viscosity is limited within the BBL and it is difficult for the sediments to suspend to the upper part; the stratification effects contribute to the formation as the sediment diffusivity is further decreased from turbulence damping; when currents are imposed, the SSC profiles become smother and the upper part becomes turbid. 2) we could directly establish the relation between the HCL and the BBL but it is not appropriate to relate the HCL with a single factor, for example the ripple parameters or flow parameters; the thickness of the HCL is about twice the height of the wave BBL. 3) Bed forms determine the shape of the concentration profile near the bottom, and flow dynamics determine the magnitude. Different approaches have to be employed to simulate the sediment concentration under different bed forms. 4) For finer sediment, the mobile bed effects and hindered settling are non-ignorable factors.

The simulation of the HCL helps us better understand the vertical concentration distributions of silt-dominated sediment under different wave-current conditions. It is a supplemental tool to flume experiments and a forerunner of 3D simulations. Meanwhile, it can serve as a simple reference model to test theoretical formulas, or to help assess the empirical parameterizations in those formulas for 2DH/3D modelling.

In natural environments, there are generally mixtures of clay, silt and sand. Bed composition will have effects on bed forms and sediment concentration distribution. At this stage, this paper mainly studies the high concentration behavior of pure silt and very fine sandy sediments while the sediment composition was treated as uniform. It is a future study direction to simulate sediment mixtures.

Acknowledgments

Selected notation

A	Wave amplitude
B_k	Buoyancy flux
c	Sediment concentration by mass or volume
c_{gel}	Gelling volume concentration
c_a	Reference sediment concentration
c_v	Volume sediment concentration of solids
$c_{v,structure}$	Maximum volume fraction of solids
$c_{gel,s}$	Maximum volume concentration of sand bed
c_μ	Coefficient in k-ε model (= 0.09)
d	Diameter of bed material
d_{50}	Median size of sediment
d_{10}	Grain size for which 10% of the bed material is finer
d_s	Sieve diameter
d_*	Dimensionless particle size
f_w	Wave friction coefficient
g	Gravitational acceleration
h	Water depth
H	Wave height
J	Water surface slope
k	Turbulent kinetic energy
k_s	Roughness height
k_{vortex}	Turbulent kinetic energy at the edge of vortex layer
N	Brunt-Vaisala frequency
p	Water pressure
Re d_*	Non-dimensional sediment Reynolds number
Re$_{wave}$	Wave Reynolds number
s	Relative density
T	Wave period
u	Instantaneous horizontal velocity
$\bar{u}$	Mean horizontal velocity
$\tilde{u}$	Oscillatory horizontal velocity
u_c	Mean current velocity
u_m	Maximum wave orbital velocity
u_*	Shear velocity
u_w	Wave-related velocity
u_{wc}	Velocity of combined wave-current
$\tilde{u}_\infty$	Horizontal free stream velocity
w	Vertical velocity
w_s	Settling velocity
$w_{s,0}$	Settling velocity in clear fluid

z	Vertical coordinate from flat bed or ripple crest level
z_a	Reference height
z_{max}	Maximum z in the calculation domain
ε	Turbulent dissipation
ε_{vortex}	Turbulent dissipation at the edge of vortex layer
ε_s	Sediment diffusivity
ϕ_d	Damping coefficient
$\phi_{s,struct}$	Structural density
$\phi_{s,max}$	Maximum density
η	Ripple height
κ	Kaman number
λ	Ripple length
θ	Shields number
θ_c	Critical Shields number
θ_{zc}	Revised critical Shields number (Incipience number)
θ_r	Ripple-adjusted value of Shields number
υ	Kinematic viscosity coefficient
υ_t	Eddy viscosity
υ_{tN}	Eddy viscosity in vortes-dominated layer
ρ_w	Water density
ρ_s	Sediment density
ρ_m	Density of water-sediment mixture
σ_v	Prandtl-Schmidt number
τ	Shear stress
τ_c	Critical shear stress
τ_m	Maximum wave shear stress
ψ	Mobility number
ζ	Water level

Appendix A. Derivation of Reynolds equation for wave-current motions

From the simplification of the N-S equations, the governing equations in x-z coordinate are:
Momentum equation:

$$\frac{\partial u}{\partial t} + u\frac{\partial u}{\partial x} + w\frac{\partial u}{\partial z} = -\frac{1}{\rho}\frac{\partial p}{\partial x} + \upsilon\left(\frac{\partial^2 u}{\partial x^2} + \frac{\partial^2 u}{\partial z^2}\right) \tag{A1}$$

Continuity equation:

$$\frac{\partial u}{\partial x} + \frac{\partial w}{\partial z} = 0 \tag{A2}$$

where, u, w are instantaneous velocities in the x and z directions, respectively, p is the pressure, ρ is the water density, and υ is the kinetic viscosity.

Following the Reynolds' decomposition method, the Reynolds equations for wave-current BBL are obtained by splitting the variables into a fluctuating component u', an averaged component $\overline{u}$ and an oscillatory component $\widetilde{u}$.

$$u = \overline{u} + \widetilde{u} + u',$$
$$w = \overline{w} + \widetilde{w} + w',$$
$$p = \overline{p} + \widetilde{p} + p' \tag{A3}$$

The oscillatory velocity $\widetilde{u}$ is defined as: $\widetilde{u} = \frac{1}{N}\sum_{j=1}^{N} u(z, t + jT) - \overline{u(z)}$, where T is the wave period.
Taking the time-average, we obtain the momentum equation for $\overline{u}$

$$\frac{\partial \overline{u}}{\partial t} + \left[\frac{\partial \overline{u}\overline{u}}{\partial x} + \frac{\partial \overline{u}\overline{w}}{\partial z}\right] + \left[\frac{\partial \overline{\widetilde{u}\widetilde{u}}}{\partial x} + \frac{\partial \overline{\widetilde{u}\widetilde{w}}}{\partial z}\right] + \left[\frac{\partial \overline{u'u'}}{\partial x} + \frac{\partial \overline{u'w'}}{\partial z}\right] =$$
$$-\frac{1}{\rho}\frac{\partial \overline{p}}{\partial x} + \upsilon\left[\frac{\partial}{\partial x}\frac{\partial \overline{u}}{\partial x}\right] + \upsilon\left[\frac{\partial}{\partial z}\frac{\partial \overline{u}}{\partial z}\right] \tag{A4}$$

The mean Reynolds stress can be expressed as

$$-\overline{u'w'} = \overline{\upsilon}_t\frac{\partial \overline{u}}{\partial z} \tag{A5}$$

in which $\overline{\upsilon}_t$ is the eddy viscosity.
Then we get the momentum equation for the mean velocity:

$$\frac{\partial \overline{u}}{\partial t} + \frac{\partial}{\partial x}(\overline{u}\overline{u} + \overline{\widetilde{u}\widetilde{u}}) + \frac{\partial}{\partial z}(\overline{u}\overline{w} + \overline{\widetilde{u}\widetilde{w}}) = -\frac{1}{\rho}\frac{\partial \overline{p}}{\partial x} + \frac{\partial}{\partial z}\left[(\upsilon + \overline{\upsilon}_t)\frac{\partial \overline{u}}{\partial z}\right] \tag{A6}$$

in which $\frac{\partial}{\partial x}\overline{\widetilde{u}\widetilde{u}} + \frac{\partial}{\partial z}\overline{\widetilde{u}\widetilde{w}}$ is the wave-induced stress term, which is analogous to the familiar Reynolds stresses (Nielsen, 1992).

Taking the phase-average, we obtain the equation for $\tilde{u}$

$$\frac{\partial \tilde{u}}{\partial t} + \frac{\partial}{\partial x}(\bar{u}\tilde{u}) + \frac{\partial}{\partial x}(\tilde{u}\bar{u}) + \frac{\partial}{\partial z}(\bar{u}\tilde{w} + \tilde{u}\bar{w}) + \frac{\partial}{\partial x}(\widetilde{\tilde{u}\tilde{u}}) + \frac{\partial}{\partial z}(\widetilde{\tilde{u}\tilde{w}}) + \frac{\partial}{\partial x}(\widetilde{u'u'}) + \frac{\partial}{\partial z}(\widetilde{u'w'}) =$$

$$-\frac{1}{\rho}\frac{\partial \tilde{p}}{\partial x} + \upsilon \left(\frac{\partial^2 \tilde{u}}{\partial x^2} + \frac{\partial^2 \tilde{u}}{\partial z^2} \right) \tag{A7}$$

The oscillatory Reynolds stress is define as

$$-\widetilde{u'w'} = \tilde{\upsilon}_t \frac{\partial \tilde{u}}{\partial z} \tag{A8}$$

Then we get

$$\frac{\partial \tilde{u}}{\partial t} + \frac{\partial}{\partial x}(\bar{u}\tilde{u} + \tilde{u}\bar{u}) + \frac{\partial}{\partial z}(\bar{u}\tilde{w} + \tilde{u}\bar{w}) + \frac{\partial}{\partial x}(\widetilde{\tilde{u}\tilde{u}}) + \frac{\partial}{\partial z}(\widetilde{\tilde{u}\tilde{w}}) =$$

$$-\frac{1}{\rho}\frac{\partial \tilde{p}}{\partial x} + \left[\frac{\partial}{\partial x}(\upsilon + \tilde{\upsilon}_t)\frac{\partial \tilde{u}}{\partial x} + \frac{\partial}{\partial z}(\upsilon + \tilde{\upsilon}_t)\frac{\partial \tilde{u}}{\partial z} \right] \tag{A9}$$

Because $\widetilde{\tilde{u}\tilde{u}} = \tilde{u}\tilde{u} - \overline{\tilde{u}\tilde{u}}$, $\widetilde{\tilde{u}\tilde{w}} = \tilde{u}\tilde{w} - \overline{\tilde{u}\tilde{w}}$, thus,

$$\frac{\partial}{\partial x}\widetilde{\tilde{u}\tilde{u}} = \frac{\partial}{\partial x}\tilde{u}\tilde{u} - \frac{\partial}{\partial x}\overline{\tilde{u}\tilde{u}} \tag{A10}$$

$$\frac{\partial}{\partial z}\widetilde{\tilde{u}\tilde{w}} = \frac{\partial}{\partial z}\tilde{u}\tilde{w} - \frac{\partial}{\partial z}\overline{\tilde{u}\tilde{w}} \tag{A11}$$

We finally get the momentum equation for oscillatory motion

$$\frac{\partial \tilde{u}}{\partial t} + \frac{\partial}{\partial x}(\bar{u}\tilde{u} + \tilde{u}\bar{u} + \tilde{u}\tilde{u} - \overline{\tilde{u}\tilde{u}}) + \frac{\partial}{\partial z}(\bar{u}\tilde{w} + \tilde{u}\bar{w} + \tilde{u}\tilde{w} - \overline{\tilde{u}\tilde{w}}) = -\frac{1}{\rho}\frac{\partial \tilde{p}}{\partial x} + \frac{\partial}{\partial z}\left[(\upsilon + \tilde{\upsilon}_t)\frac{\partial \tilde{u}}{\partial z} \right] \tag{A12}$$

The time scale in the Reynolds equation is much smaller than the oscillatory period but much larger than turbulence. Then, ignore the fluctuating components, $U = \bar{u} + \tilde{u}$, $P = \bar{p} + \tilde{p}$, where U and P represent Reynolds averaged components which are the sums of the averaged values and the oscillatory values. Let $\bar{\upsilon}_t \frac{\partial \bar{u}}{\partial x} + \tilde{\upsilon}_t \frac{\partial \tilde{u}}{\partial x} = \upsilon_t \frac{\partial(\bar{u}+\tilde{u})}{\partial x}$, in which $\upsilon_t = \left(\bar{\upsilon}_t \frac{\partial \bar{u}}{\partial x} + \tilde{\upsilon}_t \frac{\partial \tilde{u}}{\partial x} \right) / \frac{\partial(\bar{u}+\tilde{u})}{\partial x}$. By combining the time-averaged (Eq. (A6)) and phase-averaged equations (Eq. (A12)), we get the Reynolds equations for the wave-current BBL, Eq. (A13). To simplify, we rewrite U as u and P as p in the following equations.

Momentum equation

$$\frac{\partial u}{\partial t} + u\frac{\partial u}{\partial x} + w\frac{\partial u}{\partial z} = -\frac{1}{\rho}\frac{\partial p}{\partial x} + \frac{\partial}{\partial z}\left[(\upsilon + \upsilon_t)\frac{\partial u}{\partial z} \right] \tag{A13}$$

Similarly, the continuity equation is

$$\frac{\partial u}{\partial x} + \frac{\partial w}{\partial z} = 0 \tag{A14}$$

Appendix B. Time varying functions of the eddy viscosity and the reference concentration (Davies and Thorne, 2005)

The time varying eddy viscosity is assumed to be given by the real part of the following expression,

$$\upsilon_{tN}(t) = \overline{\upsilon_{tN}}f(\omega t) \tag{B1}$$

With $f(\omega t) = (1 + \varepsilon_0 + \varepsilon_1 e^{i\omega t} + \varepsilon_2 e^{2i\omega t})$ $\qquad$ (B2)

In witch $\varepsilon_1 = |\varepsilon_1|e^{i\varphi_1}$,

$$\varepsilon_2 = |\varepsilon_2|e^{i\varphi_2} \tag{B3}$$

For asymmetrical wave motion, the asymmetry parameter $B = |u_2/u_1|$ is defined at the edge of the wave boundary layer by

$$u_\infty = u_1 e^{i\omega t} + u_2 e^{2i\omega t} \tag{B4}$$

$$|\varepsilon_1| = \begin{cases} 10B & B \leq 0.1 \\ 1.0 & B \geq 0.1 \end{cases} \tag{B5}$$

$$|\varepsilon_2| = \begin{cases} 1.0 & B \leq 0.1 \\ 1.0 - \frac{40}{3}(B - 0.1) & 0.1 \leq B \leq 0.15 \\ 1/3 & B \geq 0.15 \end{cases} \tag{B6}$$

$$\varepsilon_0 = |\varepsilon_1|^2/(8|\varepsilon_2|) \tag{B7}$$

Davies and Thorne (2005) found that the peak eddy viscosity occurs just before flow reversal. The following phase relationships are used for the components of the eddy viscosity in relation to the instant of flow reversal following the passage of the wave crest,

$$\varphi_2 = 2\varphi_1,$$
$$\varphi_1 = -\arccos(B) + \Delta\varphi \tag{B8}$$

with the phase lead of the peak eddy viscosity before flow reversal corresponding to $\Delta\varphi = 4°$.

The time-varying reference concentration over rippled bed is

$$c_a(t) = \overline{c_a} \frac{0.5((1 + \varepsilon_0) + \varepsilon_1 e^{iwt} + \varepsilon_2 e^{2iwt})((1 + a_c e^{2iwt}) + c.c)}{((1 + \varepsilon_0) + 0.25 A_c |\varepsilon_0| (e^{i(2\phi_1 - 2\phi_c)} + c.c))} \tag{B9}$$

where $\overline{c_a}$ is the mean reference sediment concentration. $A_c = 1$. The coefficient $a_c = A_c \exp(2i\varphi_c)$. c.c. denotes the complex conjugate. The phase angle φ_c is taken as $\varphi_c = \varphi_1 + 30 \times (\pi/180)$ which corresponds to $\varphi_c \approx 34°$ and leads to the outcome that the predicted concentration maxima at the crest level occur somewhat before flow reversal.

References

Baas, J.H., Best, J.L., Peakall, J., 2016. Predicting bedforms and primary current stratification in cohesive mixtures of mud and sand. J. Geol. Soc. 173 (1), 12–45.

Bagnold, R.A., Taylor, G., 1946. Motion of waves in shallow water. Proc. Roy. Soc. Lond. Math. Phys. Sci. 1–15.

Baldock, T.E., Tomkins, M.R., Nielsen, P., Hughes, M.G., 2004. Settling velocity of sediments at high concentrations. Coast Eng. 51 (1), 91–100.

Camenen, B., Larson, M., Bayram, A., 2009. Equivalent roughness height for plane bed under oscillatory flow. Estuar. Coast Shelf Sci. 81 (3), 409–422.

Cao, Z.D., Yang, S.S., Yang, H., 2009. Definition of silt-sandy beach and its characteristics of sediment movement. Port & Waterway Engineering (5), 1–4 (in Chinese with English abstract).

Conley, D.C., Falchetti, S., Lohmann, I.P., Brocchini, M., 2008. The effects of flow stratification by non-cohesive sediment on transport in high-energy wave-driven flows. J. Fluid Mech. 610, 43–67.

Davies, A.G., Thorne, P.D., 2005. Modeling and measurement of sediment transport by waves in the vortex ripple regime. J. Geophys. Res.: Oceans (1978–2012) 110 (C05017), 1–25.

Davies, A.G., Villaret, C., 1999. Eulerian drift induced by progressive waves above rippled and very rough beds. J. Geophys. Res.: Oceans 104 (C1), 1465–1488.

Davies, A.G., Villaret, C., 2002. Prediction of sand transport rates by waves and currents in the coastal zone. Continent. Shelf Res. 22 (18), 2725–2737.

Davies, A.G., Villaret, C., 2003. Sediment transport modelling for coastal morphodynamics. In: Proceedings of coastal sediments. Citeseer, pp. 18–23.

Deigaard, R., Jakobsen, J.B., Fredsøe, J., 1999. Net sediment transport under wave groups and bound long waves. J. Geophys. Res.: Oceans 104 (C6), 13559–13575.

Dingler, J.R., Inman, D.L., 1976. Wave-formed ripples in nearshore sands. Coast Eng. Proc. 13, 2109–2126.

Dohmen Janssen, C.M., Hassan, W.N., Ribberink, J.S., 2001. Mobile-bed effects in oscillatory sheet flow. J. Geophys. Res.: Oceans (1978–2012) 106 (C11), 27103–27115.

Dohmen-Janssen, C.M., Kroekenstoel, D.F., Hassan, W.N., Ribberink, J.S., 2002. Phase lags in oscillatory sheet flow: experiments and bed load modelling. Coast Eng. 46 (1), 61–87.

Dong, P., Sato, S., Liu, H., 2013. A sheetflow sediment transport model for skewed-asymmetric waves combined with strong opposite currents. Coast Eng. 71, 87–101.

Fredsøe, J., 1984. Sediment Transport in Current and Waves. Institute of Hydrodynamics and Hydraulic Engineering. Technical University of Denmark.

Fredsøe, J., Deigaard, R., 1992. Mechanics of Coastal Sediment Transport, 3. World Scientific.

Fredsøe, J., Andersen, K.H., Sumer, B.M., 1999. Wave plus current over a ripple-covered bed. Coast Eng. 38 (4), 177–221.

Grant, W.D., Madsen, O.S., 1979. Combined wave and current interaction with a rough bottom. J. Geophys. Res.: Oceans (1978–2012) 84 (C4), 1797–1808.

Grant, W.D., Madsen, O.S., 1982. Movable bed roughness in unsteady oscillatory flow. J. Geophys. Res.: Oceans (1978–2012) 87 (C1), 469–481.

Grant, W.D., Williams III, A.J., Glenn, S.M., 1984. Bottom stress estimates and their prediction on the northern California continental shelf during CODE-1, the importance of wave-current interaction. J. Phys. Oceanogr. 14 (3), 506–527.

Grasmeijer, B.T., Kleinhans, M.G., 2004. Observed and predicted bed forms and their effect on suspended sand concentrations. Coast Eng. 51 (5), 351–371.

Groenenboom, J., 2015. Modelling Sand-mud-bed Interaction in the Scheldt Estuary (Master Thesis). Delft University of Technology, Delft, The Netherlands.

Guizien, K., Dohmen Janssen, M., Vittori, G., 2003. 1DV bottom boundary layer modeling under combined wave and current: turbulent separation and phase lag effects. J. Geophys. Res.: Oceans (1978–2012) 108 (C11), 3016.

Hassan, W., Ribberink, J.S., 2010. Modelling of sand transport under wave-generated sheet flows with a RANS diffusion model. Coast. Eng. 57 (1), 19–29.

Henderson, S.M., Allen, J.S., Newberger, P.A., 2004. Nearshore sandbar migration predicted by an eddy-diffusive boundary layer model. J. Geophys. Res.: Oceans (1978–2012) 109 (C6) C06024.

Holmedal, L.E., Myrhaug, D., 2006. Boundary layer flow and net sediment transport beneath asymmetrical waves. Continent. Shelf Res. 26 (2), 252–268.

Holmedal, L.E., Myrhaug, D., 2009. Wave-induced steady streaming, mass transport and net sediment transport in rough turbulent ocean bottom boundary layers. Continent. Shelf Res. 29 (7), 911–926.

Holmedal, L.E., Myrhaug, D., Eidsvik, K.J., 2004. Sediment suspension under sheet flow conditions beneath random waves plus current. Continent. Shelf Res. 24 (17), 2065–2091.

Hooshmand, A., Horner-Devine, A.R., Lamb, M.P., 2015. Structure of turbulence and sediment stratification in wave-supported mud layers. J. Geophys. Res.: Oceans 120 (4), 2430–2448.

Hsu, T.J., Ozdemir, C.E., Traykovski, P.A., 2009. High-resolution numerical modeling of wave-supported gravity-driven mudflows. J. Geophys. Res.: Oceans 114 (C5) C05014.

Hsu, T.W., Ou, S.H., 1994. On the mass transport of water waves in a turbulent boundary layer. Ocean Eng. 21 (2), 195–206.

Jensen, B.J., Sumer, B.M., Fredsoe, J., 1989. Turbulent oscillatory boundary layers at high Reynolds numbers. J. Fluid Mech. 206 (206), 265–297.

Khelifa, A., Ouellet, Y., 2000. Prediction of sand ripple geometry under waves and currents. J. Waterw. Port, Coast. Ocean Eng. 126 (1), 14–22.

Kineke, G.C., Sternberg, R.W., Trowbridge, J.H., Geyer, W.R., 1996. Fluid-mud processes on the Amazon continental shelf. Continent. Shelf Res. 16 (5), 667–696.

Klopman, G., 1994. Vertical Structure of the Flow Due to Waves and Currents: Laser-Doppler Flow Measurements for Waves Following or Opposing a Current, Delft Hydraulic Laboratory Report H840, Delft, The Netherlands.

Kranenburg, W.M., Ribberink, J.S., Schretlen, J.J., Uittenbogaard, R.E., 2013. Sand transport beneath progressive waves: the role of progressive wave streaming and other free surface effects. J. Geophys. Res.: Earth Surface 118 (1), 122–139.

Kranenburg, W.M., Ribberink, J.S., Uittenbogaard, R.E., Hulscher, S.J., 2012. Net currents in the wave bottom boundary layer: on waveshape streaming and progressive wave streaming. J. Geophys. Res.: Earth Surface (2003–2012) 117 F03005.

Lamb, M.P., Parsons, J.D., 2005. High-density suspensions formed under waves. J. Sediment. Res. 75 (3), 386–397.

Li, S., 2014. Turbulent Structure and Sediment Alluvial Process in Wave-current Boundary Layer. Nanjing Hydraulic Research Institute, Nanjing, China (in Chinese).

Mehta, A.J., Lee, S., 1994. Problems in linking the threshold condition for the transport of cohesionless and cohesive sediment grain. J. Coast. Res. 10 (1), 170–177.

Mogridge, G.R., Davies, M.H., Willis, D.H., 1994. Geometry prediction for wave-generated bedforms. Coast Eng. 22 (3), 255–286.

Myrhaug, D., Holmedal, L.E., 2007. Mobile layer thickness in sheet flow beneath random waves. Coast Eng. 54 (8), 577–585.

Nielsen, P., 1992. Coastal Bottom Boundary Layers and Sediment Transport. Advanced Series on Ocean Engineering, vol. 4 World Scientific, Singapore.

O'Donoghue, T., Wright, S., 2004. Flow tunnel measurements of velocities and sand flux in oscillatory sheet flow for well-sorted and graded sands. Coast Eng. 51 (11), 1163–1184.

Ribberink, J.S., Al Salem, A.A., 1994. Sediment transport in oscillatory boundary layers in cases of rippled beds and sheet flow. J. Geophys. Res.: Oceans (1978–2012) 99 (C6), 12707–12727.

Ribberink, J.S., Al-Salem, A.A., 1995. Sheet flow and suspension of sand in oscillatory boundary layers. Coast Eng. 25 (3), 205–225.

Ribberink, J.S., van der Werf, J.J., O'Donoghue, T., Hassan, W.N.M., 2007. Sand Motion Induced by Oscillatory Flows: Sheet Flow and Vortex Ripples. Particle-laden Flow. Springer, The Netherlands, pp. 1–32.

Richardson, J.F., Zaki, W.N., 1954. Sedimentation and fluidization: Part I. Trans. Inst. Chem. Eng. 32, 35–53.

Roberts, J., Jepsen, R., Gotthard, D., Lick, W., 1998. Effects of particle size and bulk density on erosion of quartz particles. J. Hydraul. Eng. 124 (12), 1261–1267.

Ruessink, B.G., Van den Berg, T., Van Rijn, L.C., 2009. Modeling sediment transport beneath skewed asymmetric waves above a plane bed. J. Geophys. Res.: Oceans 114 C11021.

Sana, A., Ghumman, A.R., Tanaka, H., 2007. Modification of the damping function in the k-ε model to analyse oscillatory boundary layers. Ocean Eng. 34 (2), 320–326.

Sanford, L.P., 2008. Modeling a dynamically varying mixed sediment bed with erosion, deposition, bioturbation, consolidation, and armoring. Comput. Geosci. 34 (10), 1263–1283.

Smith, J.D., McLean, S.R., 1977. Spatially averaged flow over a wavy surface. J. Geophys. Res. 82 (12), 1735–1746.

Stive, M.J., De Vriend, H.J., 1994. Shear stresses and mean flow in shoaling and breaking waves. Coast Eng. Proc. ASCE 594–608.

Styles, R., Glenn, S.M., 2003. A theoretical investigation of bed-form shapes. Ocean Dynam. 53 (3), 278–287.

Tanaka, H., Thu, A., 1994. Full-range equation of friction coefficient and phase difference in a wave-current boundary layer. Coast Eng. 22 (3), 237–254.

Te Slaa, S., He, Q., van Maren, D.S., Winterwerp, J.C., 2013. Sedimentation processes in silt-rich sediment systems. Ocean Dynam. Theoretical, Computational and Observational Oceanography 63 (4), 399–421.

Te Slaa, S., van Maren, D.S., He, Q., Winterwerp, J.C., 2015. Hindered settling of silt. J. Hydraul. Eng. 141 (9), 04015020.

Thorne, P.D., Williams, J.J., Davies, A.G., 2002. Suspended sediments under waves measured in a large-scale flume facility. J. Geophys. Res. 107 (C8), 3178.

Traykovski, P., Wiberg, P.L., Geyer, W.R., 2007. Observations and modeling of wave-supported sediment gravity flows on the Po prodelta and comparison to prior observations from the Eel shelf. Continent. Shelf Res. 27 (3), 375–399.

Trowbridge, J., Madsen, O.S., 1984. Turbulent wave boundary layers: 1. Model formulation and first-order solution. J. Geophys. Res.: Oceans (1978–2012) 89 (C5), 7989–7997.

Trowbridge, J.H., Kineke, G.C., 1994. Structure and dynamics of fluid muds on the Amazon continental shelf. J. Geophys. Res.: Oceans 99 (C1), 865–874.

Uittenbogaard, R., Bosboom, J., van Kessel, T., 2001. Numerical Simulation of Wave-current Driven Sand Transport. WL| Delft Hydraulics (Deltares), Delft, The Netherlands.

Uittenbogaard, R.E., Bosboom, J., Kessel, T.V., 2000. Numerical Simulation of Wave-current Driven Sand Transport: Theoretical Background of the Beta-release of the POINT-sand Model. WL| Delft Hydraulics (Deltares), Delft, The Netherlands.

Umeyama, M., 2005. Reynolds stresses and velocity distributions in a wave-current co-existing environment. J. Waterw. Port, Coast. Ocean Eng. 131 (5), 203–212.

van der A, D.A., 2005. 1DV Modelling of Wave-induced Sand Transport Processes over Rippled Beds. Master thesis. University of Twente, Enschede, The Netherlands.

van Der Werf, J.J., 2003. A Literature Review on Sand Transport under Oscillatory Flow Conditions in the Rippled-bed Regime, Universty of Twente. Enschede, The Netherlands.

van der Werf, J.J., Ribberink, J.S., O'Donoghue, T., Doucette, J.S., 2006. Modelling and measurement of sand transport processes over full-scale ripples in oscillatory flow. Coast Eng. 53 (8), 657–673.

van Maren, D.S., Winterwerp, J.C., Wang, Z.Y., Pu, Q., 2009. Suspended sediment dynamics and morphodynamics in the Yellow River, China. Sedimentology 56 (3), 785–806.

van Rijn, L.C., 1993. Principles of Sediment Transport in Rivers, Estuaries and Coastal Seas, 1006. Aqua publications Amsterdam, The Netherlands.

van Rijn, L.C., 2007a. Unified view of sediment transport by currents and waves. II: suspended transport. J. Hydraul. Eng. 133 (6), 668–689.

van Rijn, L.C., 2007b. Unified view of sediment transport by currents and waves. I: initiation of motion, bed roughness, and bed-load transport. J. Hydraul. Eng. 133 (6), 649–667.

Wilson, K.C., 1989. Friction of wave-induced sheet flow. Coast Eng. 12 (4), 371–379.

Winterwerp, J.C., 1999. On the Dynamics of High-concentrated Mud Suspensions, TU Delft. Delft University of Technology, Delft, The Netherlands.

Winterwerp, J.C., 2001. Stratification effects by cohesive and noncohesive sediment. J. Geophys. Res.: Oceans (1978–2012) 106 (C10), 22559–22574.

Winterwerp, J.C., 2002. On the flocculation and settling velocity of estuarine mud. Continent. Shelf Res. 22 (9), 1339–1360.

Winterwerp, J.C., Uittenbogaard, R.E., 1997. Sediment Transport and Fluid Mud Flow: Physical Mud Properties and Parameterization of Vertical Transport Processes SILTMAN; Set-up of a POINT-mud MODEL. Deltares (WL), Delft, The Netherlands.

Yao, P., Su, M., Wang, Z., van Rijn, L.C., Zhang, C., Chen, Y., Stive, M., 2015. Experiment inspired numerical modeling of sediment concentration over sand-silt mixtures. Coast Eng. 105, 75–89.

Zhang, C., Zheng, J., Wang, Y., Zhang, M., Jeng, D., Zhang, J., 2011a. A process-based model for sediment transport under various wave and current conditions. Int. J. Sediment Res. 26 (4), 498–512.

Zhang, C., Zheng, J., Wang, Y., Demirbilek, Z., 2011b. Modeling wave-current bottom boundary layers beneath shoaling and breaking waves. Geo Mar. Lett. 31 (3), 189–201.

Zhou, Y., Ju, L., 2007. Test Study on the Characteristics of a Wind-flow-wave Flume and Sediment Movement under Wave Conditions. Nanjing Hydraulic Research Institute, Nanjing, China (in Chinese).

Zuo, L., Roelvink, D., Lu, Y., Li, S., 2017. On incipient motion of silt-sand under combined action of waves and currents. Appl. Ocean Res. 69, 116–125.

Zyserman, J.A., Fredsøe, J., 1994. Data analysis of bed concentration of suspended sediment. J. Hydraul. Eng. 120 (9), 1021–1042.